The density in the accretion disk of the active galactic nucleus Arakelian 120: A Markov chain Monte Carlo analysis of relativistic reflections

Bachelorarbeit aus der Physik

Vorgelegt von
Philipp Weber
13.11.2017

Dr. Karl Remeis Sternwarte Bamberg
Friedrich-Alexander-Universität Erlangen-Nürnberg

Betreuer: Prof. Dr. Jörn Wilms

Abstract

We present Markov chain Monte Carlo analysis of relativistic features in the X-ray spectrum of the active galactic nucleus **Arakelian 120** which is known to show the cleanest spectrum of all active galactic nuclei discovered so far. The data were taken by the *XMM-Newton* and *NuSTAR* satellites in simultaneous observations covering an energy range of $0.15\,\text{keV} - 79\,\text{keV}$. We modelled the data using the recently developed **relxilllpD** model, which accounts for relativistic effects of the supermassive black hole on the accretion disk. In contrast to other commonly used relativistic reflection models this version of the relxill model provides the density of the accretion as a free parameter. We can show that the highest probability for the density of the accretion disk is at $10^{16.12}$ particles per cm^3 which is about a magnitude higher than 10^{15} particles per cm^3 as assumed by previous relativistic reflection models.

Zusammenfassung

Wir präsentieren eine Markov Chain Monte Carlo Analyse der relativistischen Features im Röntgen-Spektrum des aktiven Galaxiekerns **Arakelian 120**, welcher dafür bekannt ist, eines der saubersten Spektren von allen bisher entdeckten aktiven Galaxiekernen zu zeigen. Die Daten wurden von den Satelliten *XMM-Newton* und *NuSTAR* in simultanen Beobachtungen erfasst, welche den Energiebereich von $0.15\,\mathrm{keV} - 79\,\mathrm{keV}$ abdecken. Wir modellieren die Daten unter Verwendung des vor Kurzem entwickelten **relxilllpD** Modells, welches relativistische Effekte des supermassiven schwarzen Lochs auf die Akkretionsscheibe berücksichtigt. Im Gegensatz zu anderen, häufig verwendeten Modellen für relativistische Reflexionen, stellt diese Version des relxill Modells die Dichte der Akkretionsscheibe als freien Parameter bereit. Wir können zeigen, dass die höchste Wahrscheinlichkeit für die Dichte der Akkretionsscheibe bei $10^{16.12}$ Partikeln pro cm^3 liegt, was etwa eine Größenordnung höher ist als 10^{15} Partikel pro cm^3, wie es von Modellen für relativistische Reflexionen zuvor angenommen wurde.

Contents

1 Introduction

When Albert Einstein published his famous Theory of General Relativity in 1915 it only was a hypothetical formulation of how massive objects can influence a construction called spacetime simply by its presence. According to the field equations the trajectories of other objects then is determined by the curvature of Spacetime. A year later in 1916 Karl Schwarzschild gave a possible solution for the field equations consisting of a metric which made it possible to describe the behaviour of spacetime in presence of a point mass. As a result closed regions in spacetime could be possible the inside of which can not interact with the surrounding in any form. Since the so called Schwarzschild metric did not include rotation the resulting object would be a perfect sphere. Also there is no possible way for information and matter to propagate from the inside to the outside. Because these, up to this point, theoretical objects would represent a perfectly dark entity in the universe they are now referred to as black holes. But it was not clear if black holes exist and if so how they would manifest themselves.

In 1943 Carl Seyfert published a paper in which he summarized the observations of nearby galaxies with bright nuclei. He also reports evidence for comparatively broad emission lines arising from the center of these galaxies.

Observations in other wavelengths confirmed Seyfert's view of these **Active Galactic**

Figure 1.1: Multi wavelength composite of the AGN Centaurus A (Credit: ESO/WFI (Optical); MPIfR/ESO/APEX/A.Weiss et al. (Submillimetre); NASA/CXC/CfA/R.Kraft et al. (X-ray) Derivative work including grading and crop: Julian Herzog)

Nuclei (**AGN**). By comparing different observations of a variety of AGN, other aspects of these sources became visible. An outstanding feature of some AGN are jets which are visible in the radio band and can extend far beyond the border of their hosting galaxies (an outstanding example is Centaurus A, see Fig. 1.1). Seyfert also divided the whole class of AGN into subclasses with respect to their spectral behaviour. In honor of his work AGN are also referred to as **Seyfert Galaxies** divided up into different **Seyfert types**. The process which caused this radiation and the jets was not clear for a long time. In 1964 Edwin Salpeter and Yakov Zel'Dovich were the first to suggest accretion mechanisms caused by **Supermassive Black Holes** (SMBH) at the center of AGN to be a possible explanation for the phenomena observed.

The first X-ray missions in the 1970s led to the result that AGN also are extremely bright sources in the X-ray regime which is in agreement with the idea of SMBH powered accretion.

The fact that these outstanding objects show different kind of emission in all wavelength bands arising from various radiation generating mechanisms renders them one of the most interesting classes of sources in modern astronomy.

In this work we focus on the influence of relativistic effects in the direct vicinity of supermassive black holes on X-ray emission. The basic properties of active galactic nuclei and a short description about the unified model which aims to describe all active galactic nuclei with a unique scenario is given in chapter 2. In order to understand the radiation processes common scenarios and the influence of relativistic effects are explained in chapter 3 where also a comprehensive model for the observed features is developed. Describing the observed spectrum with a complicated model including relativistic effects may lead to parameter degeneracy thus we use Markov chain Monte Carlo analysis to derive probability distributions over the whole parameter space. The numerical aspects of this mechanism is described in chapter 4. Observations of X-ray emission have to be carried out in space by satellites. For the analysis we make use of data measured with the *XMM-Newton* and *NuSTAR* satellites. An overview of these spacecraft, their instruments and the steps which are necessary to derive a spectrum of an X-ray source is given in chapter 5. By modelling the measured X-ray spectrum with a model that takes intrinsic parameters of AGN into account, such as the spin of the black hole, the height of a primary X-ray source above the event horizon and the density of the accretion disk, we obtain probability distributions for all parameters of the source Arakelian 120. The source of interest, Arakelian 120, and its fundamental properties is described in chapter 6 followed by the determined parameter probability distributions and confidence maps. Finally chapter 8 gives a short discussion about the results obtained in this thesis.

2 The Unified Model of Active Galactic Nuclei

Even if the classes of AGN show different spectral behaviour one of the biggest aims in research is to break down the radiation processes and therefore the structure of these objects into a common model for possibly all sources. By taking into account different parameters of host galaxies and observational influences, i.e., viewing angle, absorption features, it is possible to develop a common model.

Radio observations made clear that a feature present in about 10% of known AGN are radio jets extending far beyond the galaxies border itself. Thus the two subclasses of **radio-loud** and **radio-quiet** are characterized by this feature. Wilson & Colbert (1995) suggest that the main differences of the two types with respect to observations are

- Radio jets and lobes which are observed in radio-loud AGN and give raise to a significant fraction of the bolometric luminosity, whereas in radio-quiet sources this property is energetically insignificant

- The host galaxy which in the case of radio-loud galaxies turns out to be of the elliptical type due to recent mergers but radio-quiet ones are located in spiral galaxies

- The space density which is about 10 times higher for radio-quiet AGN at a given optical luminosity

By making use of spectral behaviour in the optical range AGN can also be characterized into different subgroups which are called **Seyfert-Galaxies** in honor of Carl Seyfert and his leading work on this topic

- **Seyfert I:** This category of galaxies feature broad hydrogen lines and narrow forbidden lines corresponding to Helium, Oxygen and Hydrogen (Osterbrock & Pogge, 1985). Antonucci (1993) also conclude that a significant portion of energy is emitted in the X-ray regime.

  (Seyfert I galaxies with point like appearance, e.g. the host galaxy is not visible, are called **Quasi Stellar Objects, Quasars**)

- **Seyfert II:** Galaxies of this type in general show no broad emission lines. In addition X-ray observations show that there is a high portion of absorption present (Burtscher et al., 2016).

The up to this point most successful model can be summarized as follows (Netzer, 2015):
In the center of the hosting galaxy exists a supermassive black hole with a mass of hundreds of thousands up to billions of solar masses. It is surrounded by a gaseous torus which outer radius is in general located at distances of kiloparsecs. The rotational axis of this structure is aligned with the rotational axis of the hosting galaxy. Different
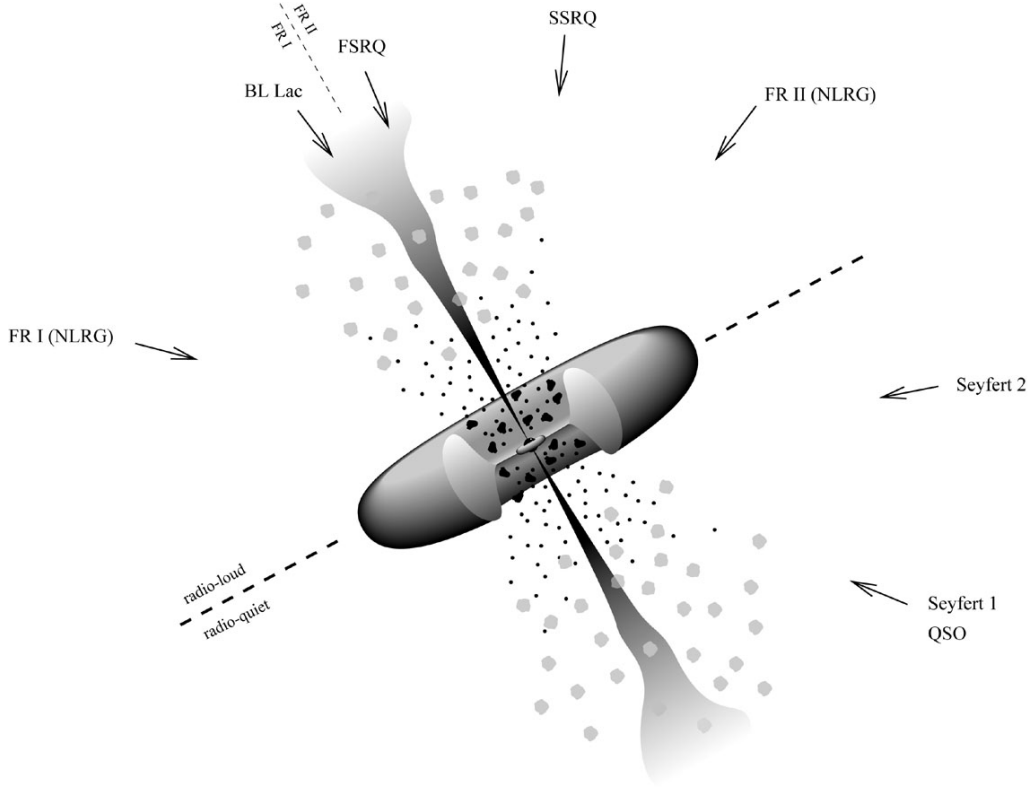
Figure 2.1: Different spectral properties of AGN can be explained by the unified model with the presence of a gaseous torus surrounding the central emission region and therefore different observational features depending on the angle between the line of sight and the plane of the accretion disk. Urry & Padovani (Taken from 1995, modified)

types of material in the torus have been discussed. Possibilities cover for example dust grains of different sizes and clumps of different density and radial distributions embedded in the structure. The inner radius is assumed to be determined by the location where dust sublimation starts to play a significant role. Since the torus is somehow extended in the direction perpendicular to the plane, the resulting opening angle also plays an important role due to the observational effects arising from radiation penetrating the absorbing medium. Because of its comparatively low temperature this outer region of the AGN is a source of narrow line emission. The overall density profile with respect to the radius is expected to have impact on dynamical processes like gas supply rate to the central region near the black hole. Due to viscosity the material is undergoing friction which increases temperature and causes an overall gas flow towards the innermost region of the torus.

By decreasing radius and increasing rotational speed the material forms a thin accretion disk as it is approaching the direct vicinity of the black hole. The outer radius of the accretion disk is assumed to be at the order of parsecs as can be shown by properties of the inner radius of the surrounding torus and dynamical simulations (Kaviraj et al., 2017). Thermal radiation of different temperatures at different radii results in a continuous su-

Figure 2.2: NGC6814 in the constellation of aquila is an intermediate spiral type galaxy hosting an AGN and is known to be a Seyfert I galaxy. Note the extraordinary bright center of the galaxy, captured in the optical and infrared (Credit: ESA/Hubble & NASA)

perposition of blackbody spectra along the elongation of the accretion disk. The resulting energy distribution of the thermal spectrum reaches from the optical to the X-rays. By reprocessing of thermal photons in scatterings of highly relativistic electrons a powerlaw across all wavelength bands is produced. Acceleration of particles in combination with magnetic fields lead to highly relativistic jets forming perpendicular to the accretion disk. Dust clouds orbiting with high speed around the central region of the overall structure are ionized by emission of the accretion disk and therefore are sources of broad lines.

The combination of the radiating black hole and geometrical structure of the dust torus cause different observational features depending on the viewing angle onto the center of the AGN (see Fig. 2.1) and can explain the different kind of AGN in a common way. If the angle between observer and the accretion disk is high an unobscured view onto the main emission source is possible. Thus the narrow line and also the broad line emission is present which corresponds to the **Seyfert I** case. In contrast if the line of sight towards the central region of the accretion disk is obscured by the extending torus the broad line emission is absorbed and only narrow line emission is present which corresponds to the **Seyfert II** type. However, even if this model is adequate for explaining spectral features of **Seyfert I** types recent observations suggest that a more complicated structure of the surrounding torus like distinct filaments, more clumpy winds and accretion flow even occurring on galactic scales.

3 Modelling the emission of AGN

The radiation emitted by AGN mainly arises from thermal processes occurring in the accretion disk in the first place. Secondary effects reprocess a significant fraction of the photons and therefore add interesting features to the overall spectrum.

3.1 Properties of black holes

The outstanding property of black holes as astronomical objects is the fact that they can be characterized by a region of spacetime which represents a border which matter can only pass in the inside direction. The first solution for an up to this point theoretical construction was given by Schwarzschild (1916) by solving the field equations developed by Einstein (1916). He derived that for a test particle of small mass in the gravitational field of another larger mass M there exists a radius r_{EH} under which no trajectories are possible any more that lead out of this region. It is given by

$$r_{\mathrm{EH}} = 2M$$

and called **Schwarzschild-radius** in honor of Karl Schwarzschild. r_{EH} is also mainly referred to as **event-horizon**. Here we apply the convention of setting the gravitational constant and the speed of light to $G = c = 1$. Therefore length and mass have the same unit which can be convenient in the following considerations. In addition there is another border r_{ms}, the radius of marginal stability, under which any particle can not establish a stable orbit:

$$r_{\mathrm{ms}} = 6M \tag{3.1}$$

If a particle passes this border in the potential field of a gravitating object it will unavoidable collide with it, or in the case of a black hole, pass the event-horizon.

According to general relativity one of the few other properties of black holes which have impact on their environment is the angular momentum, the spin. The field equations under taking account the rotation of black holes were first solved by Kerr (1963). Because of the convention mentioned above the spin J of a black hole can be expressed by its mass M and a so called **spin-parameter** a in the relation

$$J = a \cdot M$$

a can not decrease below 0 (a Schwarzschild black hole) and also not exceed 1, this represents the upper limit of a when an increase of angular momentum results in an increase of energy and therefore the mass. As a result of r_{ms} in eq. 3.1 the angular momentum of matter passing this limit is transferred directly into increasing spin of the black hole. Since the kinetic energy transferred during this process also accounts for additional mass
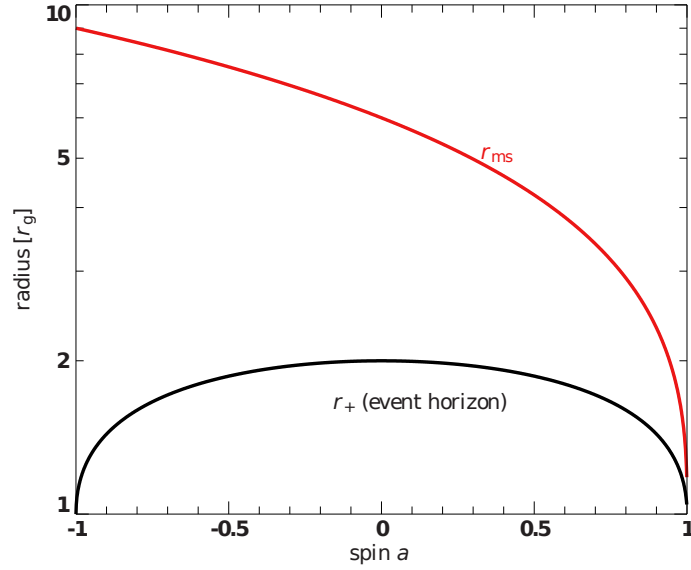
Figure 3.1: Dependence of r_{EH} and r_{ms} with respect to the spin parameter a. (Taken from Dauser, 2014, modified)

a black hole with rest mass M_i can gain more than M_i by accreting matter, in fact the additional amount of mass for a maximally spinning black hole is

$$\Delta M = 1.85 M_i$$

(Bardeen, 1970).

However, the case $a = 1$ can not be realized due to different behaviour of photons with negative spin with respect to the orientation of J compared to photons with positive spin as shown by Thorne (1974). Thus the highest expected value of a is 0.998. The sign of a refers to the spin with respect to the surrounding accretion disk, $a > 0$ means that the disk's and the black hole's angular momentum point towards the same direction, $a < 0$ denotes the opposite. Any further accretion only accounts for increasing mass.

The event-horizon of a rotating black hole is given by

$$r_{\mathrm{EH}} = M + \sqrt{M^2 - a^2} \tag{3.2}$$

which results in a smaller r_{EH} for faster spinning black holes. The same tendency is true for r_{ms}. See Fig. 3.1 for a visualization of the characteristic radii. The decreasing innermost stable circular orbit (**ISCO**) for faster spinning black holes has also impact on spectral behaviour due to different temperature and density distribution in the accretion disk.

3.2 Accretion

The mechanism making the enormous power output of AGN possible arises from matter falling towards a very compact object.

Spherical accretion: The simplest model to describe such a process assumes spherical accretion of matter onto a compact object without any additional atomic physics and was first described by Bondi (1952). Also we assume that all kinetic energy gained throughout passing the gravitational field is converted to thermal energy, resulting in thermal emission. Then the luminosity L can be derived by the accretion rate $\dot{m}$ onto a compact object with mass M to

$$L = \frac{\dot{m}MG}{R}$$

where R denotes the inner border of the accretion flow, in general given by the **ISCO**. As the radiation in the central region increases it is also necessary to take the interaction between the infalling material and the propagating photons into account. The simplest possible material to undergo such a process is hydrogen, which then experiences a gravitational force of

$$F_g = G\frac{M(m_\mathrm{p} + m_\mathrm{e})}{r^2}$$

But the interaction with the photons generates a continuous force due to the radiation onto the electrons of

$$F_\mathrm{rad} = \frac{S\sigma_\mathrm{T}}{c}$$

where $S = \frac{L}{4\pi r^2}$ is the energy flux with the luminosity L. Due to electrostatic interaction between electrons and protons, this force is also imposed onto the protons. At some point the luminosity causes the radiation pressure to hold up against the infalling material and effectively no accretion is possible any more. It is given by

$$L_\mathrm{Edd} = G\frac{4\pi M m_\mathrm{p} c}{\sigma_\mathrm{T}}$$

and called **Eddington luminosity** in honor of Sir Arthur Stanley Eddington. The mass of the electron m_e here has been neglected compared to the mass of the proton m_p in the gravitational force.

Accretion disks: The simple model of spherical accretion can not be applied to the mechanism taking place in AGN. Material reaching the inner part of the dust torus as described in chapter 2 is not spherical distributed and has a well oriented overall angular momentum. Therefore it is expected to form a disk around the black hole in the center.

   The matter in the disk be homogeneous distributed and in hydrostatic equilibrium in perpendicular direction to the plane. Also the height H of the disk is assumed to be low compared to its radius R. Then the resulting structure will have highly supersonic velocities. By taking the transport of angular momentum due to viscosity into account one can show that the resulting temperature distribution with respect to the radius is

$$T(R) \sim R^{-3/4}$$

For more detailed considerations of accretion disks see for example the original paper by
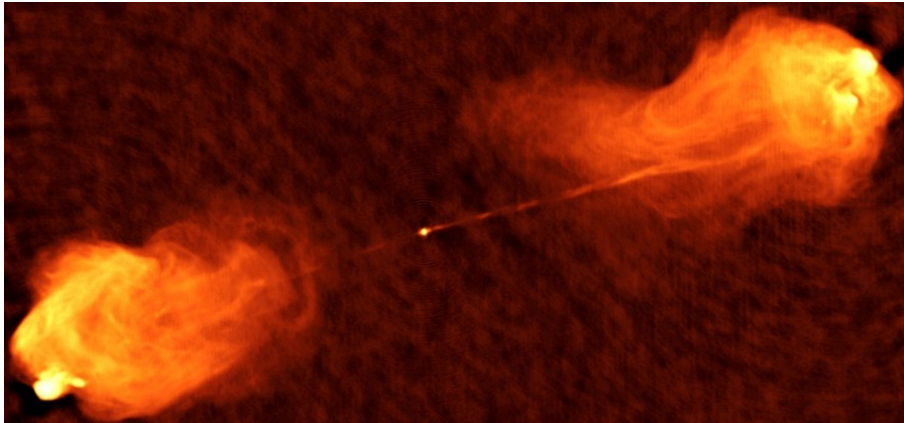
Figure 3.2: VLA observations at 4.8 GHz of Cygnus A. Radiolobes extending far beyond the galaxies borders which are produced by jets are visible. (Credit: NRAO, taken from NASA)

Shakura (1973) or for a general review Frank et al. (2002).

3.3 Relativistic Jets

Radio observations of radio loud AGN reveal extragalactic jets expelled by the hosting galaxy, an example for Cygnus A is given in Fig. 3.2[1]. The building mechanism of jets observed in AGN is not entirely clear today. Two main theories are present:

- Blandford & Znajek (1977) propose energy extraction out of a Kerr black hole being the power source for the acceleration of particles

- Blandford & Payne (1982) developed a non-relativistic model based on magnetic field lines stationary in the accretion disk which cause a „magnetic tower" over the poles of the black hole accelerating material

The presence of a relativistic jet at the poles of the central black hole is important for the evidence of a primary X-ray source which can illuminate the accretion disk and account for a reprocessed spectrum. The base of radio jets is often considered as the actual source of the primary X-ray emission (Miller et al., 2015).

3.4 Radiation processes

The simple model of a thermal accretion disk can not explain the different spectral components of AGN. Reprocessing of the incident radiation on very different components of the unified model of AGN can produce very interesting spectral features.

---

[1]Image source: https://www.nasa.gov/mission_pages/GLAST/science/blazers.html

3.4.1 Thermal emission

Due to viscosity the accretion disk described in chapter 3.2 will have very high temperatures at the inner border, reaching up to 10^8 K (Shakura, 1973). These high temperatures render the inner region of the accretion disk a source of high X-ray luminosity in the form of a blackbody spectrum over multiple temperatures. Extreme conditions in the direct vicinity of the black hole cause not only thermal instabilities (Pringle et al., 1973) but also secularly ones possibly leading to clumping of gas into rings (Lightman, 1974b,a). It has been show by Piran (1978) that the common cooling mechanisms provided by standard theory of viscosity is not sufficient for a stable accretion disk but small variations of the mathematical structure can support the inner region being the main power source.

3.4.2 Inverse Compton Scattering

The spectrum of AGN does not only show the blackbody contribution of the accretion disk itself but even mainly consists of a strong powerlaw component present in the X-ray regime (Mushotzky et al., 1993). Following Rybicki & Lightman (1986), inverse Compton scattering is assumed to be the process responsible for this spectral distribution. Photons arising from thermal radiation in the accretion disk scatter off electrons having highly relativistic energies and gain energy during this process. In comparison to the regularly observed Compton effect the energy balance is inverted since the photon gains energy. Thus this process is referred to as *inverse* Compton effect and according to models takes place in a region of hot gas surrounding the accretion disk, called **corona** (Sunyaev & Truemper, 1979). Due to the statistical properties of the collision rate the outcome of the intensity $A(E)$ for a infinite amount of incident photons is a powerlaw of the form

$$A(E) = K \cdot E^{-\Gamma}$$

where Γ is referred to as the **photon index**, determining the slope of a powerlaw in a log-log-diagram and K is a normalization parameter. For accretion disks of the form described by Shakura (1973) the intensity I of radiation scattered back onto the disk is

$$I(r) \sim r^{-3} \tag{3.3}$$

in the outer region and more constant towards the inner edge.

3.4.3 Fluorescent line emission

The abundance of iron in the interstellar medium is relatively high compared to other elements (Pinto, 2013). Therefore it also manifests itself by fluorescent line emission. Following Reynolds & Nowak (2003), high temperatures in the accretion disk ionize the iron to a certain degree which can be expressed by an ionization parameter ξ, in more detail the value of $\log(\xi)$ is often used to describe the ionization state. Since iron then is also expected to constitute a large portion of the material in the accretion disk and its Kα emission line lies with $6.4\,\text{keV}$ well in the range of sensitivity of the observing instruments it is of major interest due to its shape being distorted by a variety of effects as discussed later.
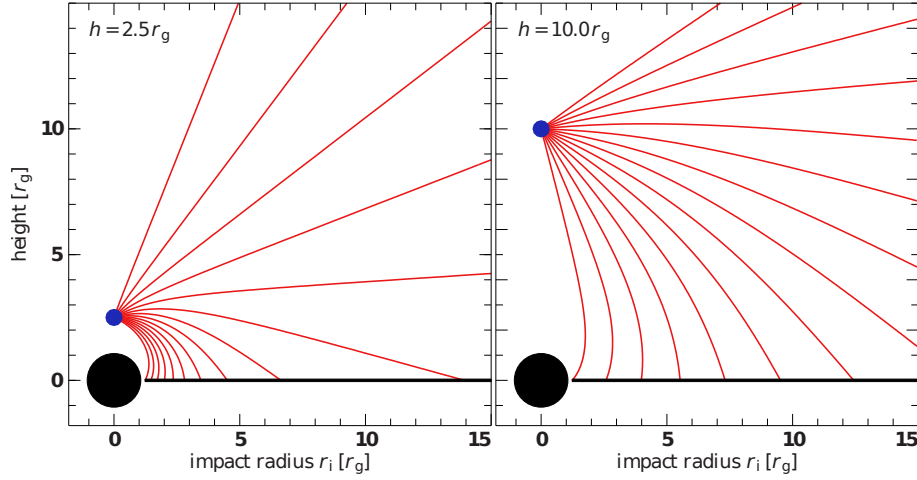
Figure 3.3: The path of photons emitted by an X-ray source sitting over the pole of a supermassive black hole is bent towards it causing higher irradiation in the inner region of the disk (Taken from Dauser, 2010)

3.5 The Lamppost structure

Radiation produced by the accretion disk in combination with a hot corona turned out not to be a sufficient assumption for a lot of sources observed. More precisely, the emissivity profile $I(r)$ in the inner region of the accretion disk turned out to be steeper (see for example Miller et al. (2002); Fabian et al. (2002, 2004)). It seemed more likely that the primary X-ray source is not sitting in the accretion disk but rather in the rotational axis of the black hole above the poles and irradiating the disk from this position. Due to this characteristics the structure is also called **Lamp post** (lamppost) structure. Ghisellini et al. (2004) have shown that basically all AGN are capable of forming jets ejecting material perpendicular to the accretion disk and that the base of this jet could represent a powerful X-ray source irradiating the accretion disk and sitting some gravitational heights r_g above the event horizon of the black hole where

$$r_g = \frac{GM}{c^2}$$

Radio-quiet AGN do not show jets on large scales which can be observed extending beyond the galaxy's border but according to this work are very likely to exist on smaller scales in the direct vicinity of the black hole but only being in that sense „aborted" that the material falls back into the event horizon due to lack of sufficient kinetic energy for full escape. The emissivity index $I(r)$ (see eq. 3.3) observed is in good agreement with the assumption of this geometry. Light bending due to curved spacetime will cause higher intensity on the inner region of the accretion disk (see Fig. 3.3) which can explain the steeper emissivity index observed (Dauser, 2010). The assumption of this geometry is well established in the field today and can explain a variety of phenomena observed.
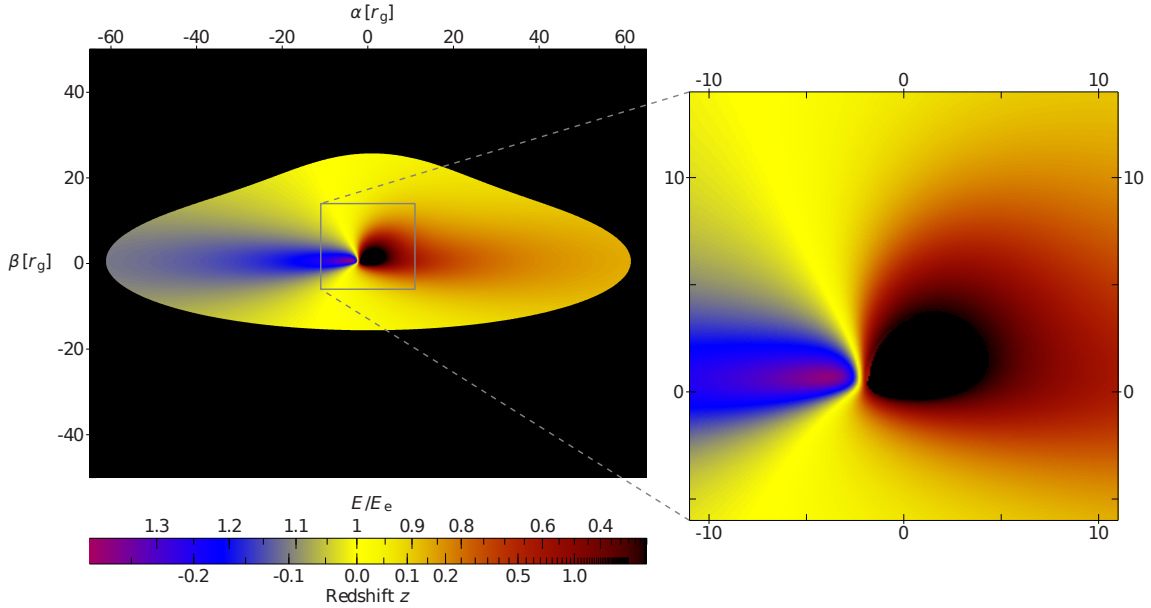
Figure 3.4: Calculation of the energy shift of radiation arising from an accretion disk around a supermassive black hole observed at an angle of $\theta = 75°$. The disk is rotating towards the observer at the left hand side. (Taken from Dauser, 2014)

3.6 Relativistic Reflections

As discussed above we assume the primary source of radiation in the X-ray band above the black hole irradiating a fast rotating accretion disk in the vicinity of a spinning black hole. This incident radiation then is reflected off the accretion disk towards the observer. Classical calculations of emission profiles would lead to wrong results in this extreme environment. First observed by Tanaka et al. (1995) for the AGN MCG−6−30−15 influence of relativistic effects onto the reflected spectrum became clear with special attention to the iron Kα line. Relativistic effects manifest themselves in different forms:

- Broadening and distortion of the iron Kα line

- Light-bending due to the mass of the black hole

- Gravitational redshift

- Blue- and redshift because of the highly relativistic moving accretion disk

All these aspects are well covered in the work of Dauser (2014), we want to develop a basic understanding of these effects based on this work.

Line Broadening and distortion: The iron Kα line is assumed to have the form of a Gaussian distribution in lab measurements. Due to the accretion disk moving at relativistic speeds near the black hole, for example $v \sim 0.3c$ for MCG−6−30−15 (Tanaka et al., 1995), the overall emission of the initially sharp line is blue-shifted on the side of the accretion
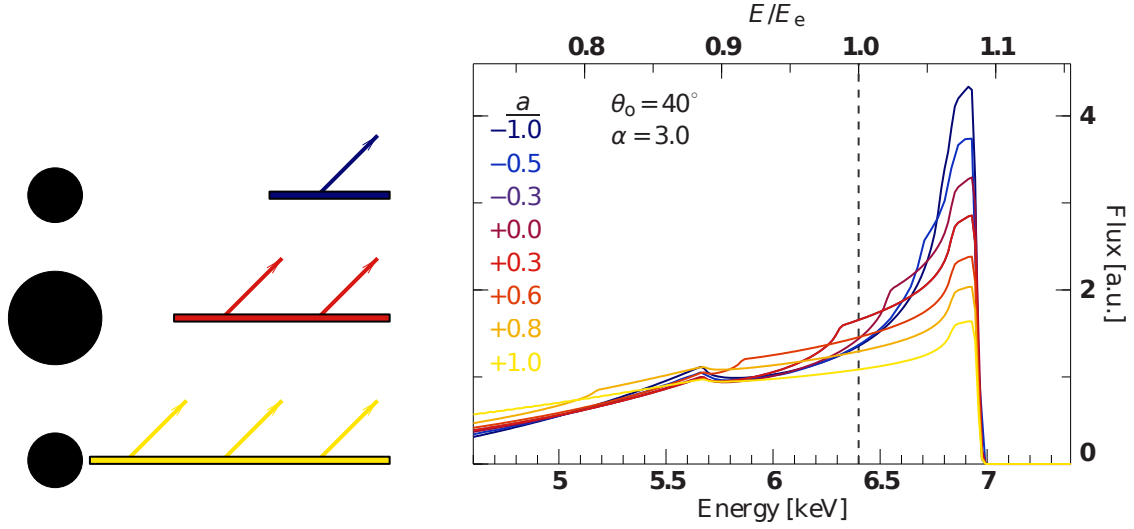
Figure 3.5: **Left:** The ISCO depends on the rotational speed of a black hole. Higher spin
means lower r_{ISCO} **Right:** Different iron $K\alpha$ line profiles for different values
of a. The higher a the wider and more distorted the line appears. Note that
also for $a = 0$ the effect is visible. (Taken from Dauser, 2014)

disk moving towards the observer and red-shifted at the other side. But also the high mass
of the black hole itself causes gravitational redshift affecting photons escaping the central
region. A calculation of the influence of both effects combined is shown in Fig. 3.4.

Light-bending: In the gravitational field of the black hole the path of light which is
emitted above the pole does not follow a straight line. Trajectories of photons are bent
towards the black hole which leads to higher intensity onto the accretion disk in the inner
region (see Fig. 3.3) and therefore also to changes in spectral properties since the emissivity
index $I(r)$ steepens towards the central object. This effect also depends on the inclination
i under which the observer looks towards the accretion disk and can distort the apparent
structure of the disk. From Fig. 3.3 one can see that the disk does not appear flat but due
to lightbending the rear part of the disk appears to be lifted. This effect depends on the
inclination i between the observer and the accretion disk.

Influence on ISCO: One of the few parameters which a black hole exposes to its environ-
ment is the spin, measured in the unit-less spin-parameter a. The ISCO also depends on
a in a quite complicated manner, see Dauser (2010), section 2.2.1 for more details. If the
disk and the black hole are rotating in the same direction ($a > 0$) r_{ISCO} can be lower than
for a Schwarzschild black hole. This leads to additional surface of the accretion disk in
the direct vicinity of the black hole and can account for a more drastic influence of energy
shift due to higher velocities. In the opposite for $a < 0$ the disk is truncated at larger radii
and therefore the effect of energy shift is expected to be less significant. Fig. 3.5 visualises
this effect and also shows the impact on the iron $K\alpha$ line.

All effects combined lead to a distorted shape of the iron $K\alpha$ line which can be observed.
See for example Fig. 3.6 which shows an analysis of 2006 data from the **Suzaku** spacecraft
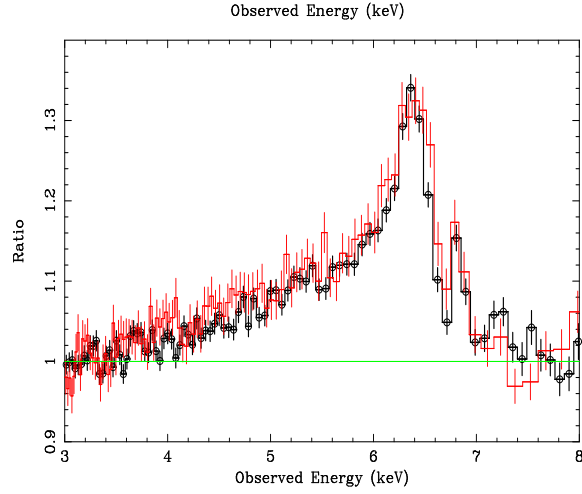
Figure 3.6: The iron Kα line of MCG-6-30-15 observed by XMM-Newton (red) and Suzaku (black). Due to relativistic effects the Gaussian shape of the emission line is not resembled. (Taken from Miniutti et al., 2007)

by Miniutti et al. (2007) combined with data from XMM-Newton.

3.7 Models

To determine the basic properties of the central black hole and surrounding material explained above we made use of mainly three models which take all spectral components of importance into account.

3.7.1 Xillver model

Xillver is a model developed by García et al. (2013) and is capable of describing the reflected spectra off an accretion disk. It does not take relativistic reflection into account. A powerlaw component can be intrinsically supported by this model, but it also offers to only represent the reflected portion. The parameters of this model are:

- *norm*: Determines the normalization parameter of this model

- Γ: The photon index of the optional powerlaw component

- A_{Fe}: The iron abundance in the accretion disk expressed in units of solar iron abundance

- E_{cut}: The energy of an „exponential cutoff" occuring at high energies ($E \sim 20 \, \text{keV} - 1 \, \text{MeV}$)

- $\log(\xi)$: The ionization state of the reflecting material as described in section 3.4.3

- z: The cosmological redshift of the source

- i: The inclination of the accretion disk with respect to the observer

- f_{refl}: The fraction between the radiation onto the disk versus the radiation reflected
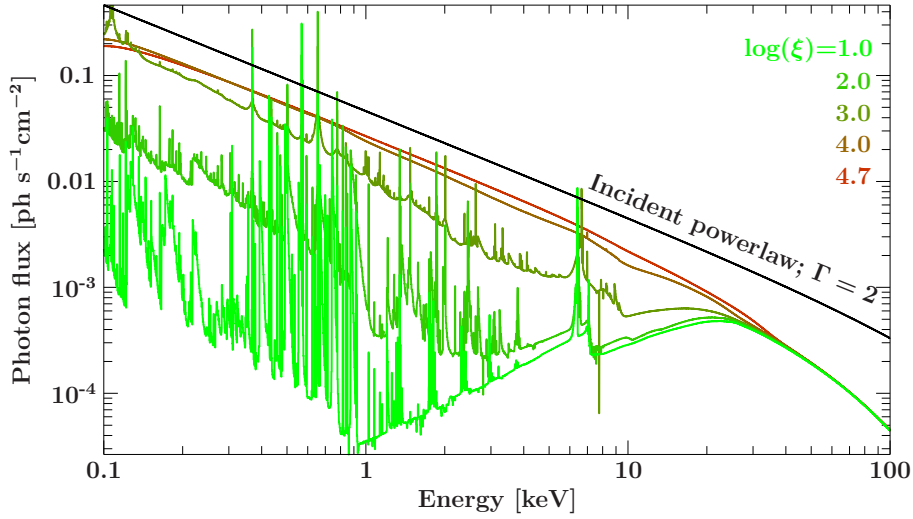
Figure 3.7: A reflection spectrum generated by xillver for different ionization states $\log(\xi)$. Only the reflected component with $f_{\mathrm{refl}} = 0.3$ is shown here. For low $\log(\xi)$ a forest of emission lines is present at low energies.

Fig. 3.7 shows the characteristics of a spectrum generated by this model in dependence of different ionization states. It is visible that for high ionization states the incident powerlaw is mainly resembled.

For further details about this model see the work of García et al. (2013) and the homepage at Harvard-Smithsonian Center for Astrophysics[2].

3.7.2 Relxill model

This model joins a relativistic ray tracing model called **relline** developed by Thomas Dauser with the xillver model described above to appropriately model X-ray reflections under relativistic conditions. It can be used in a variety of different flavours namely optionally including the lamppost structure or comptonization. Since in this work we focus on the version including the density parameter and assuming the lamppost structure, called **relxilllpD**, we only go into further detail about this flavour. It offers the following parameters:

- *norm*: The normalization constant of this model

- *h*: The height of the primary X-ray source in the lamppost structure above the event horizon. It can be expressed either in units of gravitational radii r_g or in units if the r radius of the event horizon r_{EH}

- *a*: The spin parameter of the black hole

- *i*: The inclination of the accretion disk with respect to the observer

- R_{in}: The inner radius of the accretion disk expressed in r_g

---

[2]http://hea-www.cfa.harvard.edu/ javier/xillver/
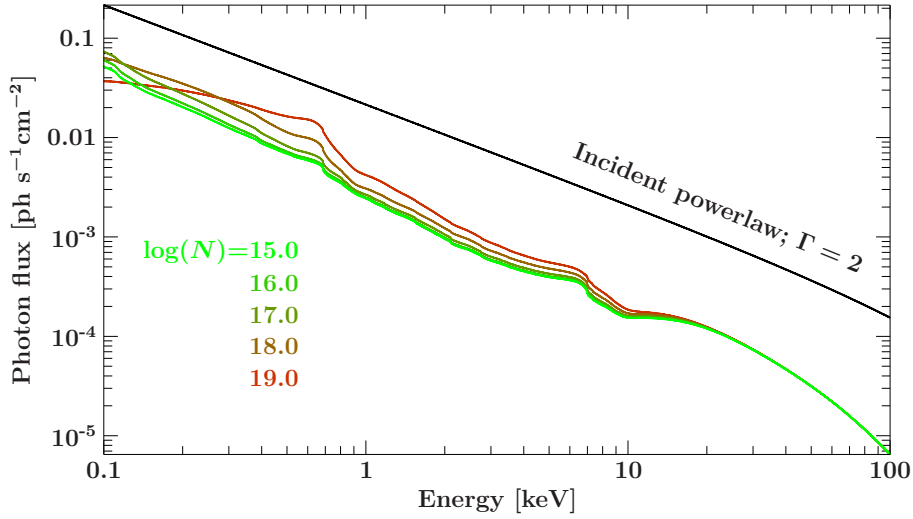
Figure 3.8: One parameter of the relxill model is the density of the material in the accretion disk expressed in logarithmical units $\log(N)$. A change in this parameter has significant impact on the form of the spectrum especially at lower energies. Only the reflected portion of the spectrum at reflection fraction f_{refl} is shown here.

- R_{out}: The outer radius of the accretion disk express in r_g

- z: The cosmological redshift of the source

- Γ: The photon index of the incident spectrum generated by the primary X-ray source of the lamppost structure

- $\log(\xi)$: The ionization parameter of the material in the accretion disk

- A_{Fe}: The iron abundance of the accretion disk expressed in solar units

- $\log(N)$: The density of the material in the accretion disk expressed in logarithmic units of 10^N particles per cm^3

- f_{refl}: The fraction between the radiation onto the disk versus the radiation reflected.

  This parameter can also be set to negative values, then only the reflected part of the spectrum is calculated and the incident powerlaw is neglected. Also the reflection fraction can be calculated from the other parameters so this parameter can be optionally varied freely.

For further details about this model see the work of Dauser (2014) and the homepage at Remeis-Observatory[3].

The special interest of this work lies on the determination of the density parameter $\log(N)$ as it is the first model allowing to determine this parameter. It is expressing the density n in terms of $n = 10^N \text{cm}^{-3}$. Fig. 3.8 shows how this parameter influences the form of the observed spectrum.

---

[3]http://www.sternwarte.uni-erlangen.de/ dauser/research/relxill/index.html
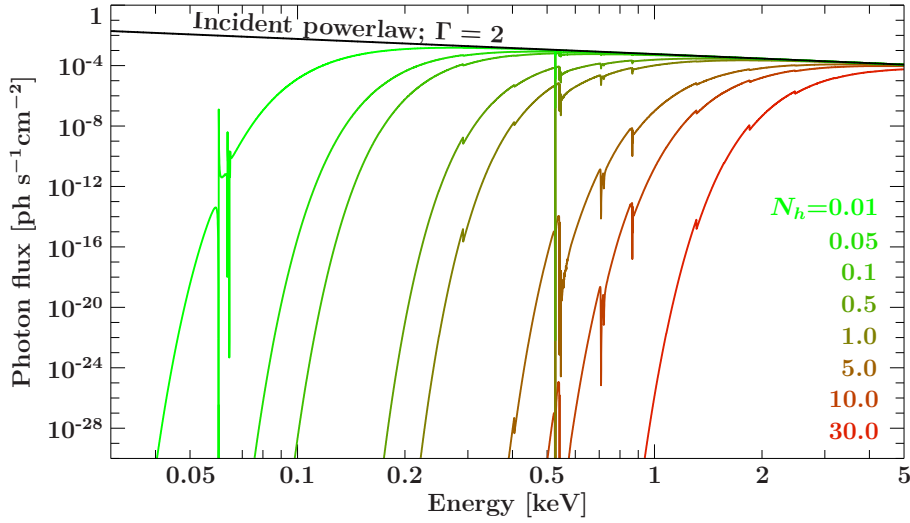
Figure 3.9: Different amount of N_H accounts for different amount of absorption. Also the impact of the absorption onto the spectrum shifts to higher energies and the absorption accounts for a variety of absorption edges. Modelled with **tbnew**

3.7.3 Absorption

The X-ray emission of AGN undergoes a significant amount of absorption due to interstellar gas in our galaxy. To take this absorption into account we use the X-ray absorption model **tbnew** developed by Wilms et al. (2000). Absorption can be parameterized by the equivalent hydrogen column density N_H which denotes the amount of hydrogen which is necessary to cause the equivalent amount of absorption measured, assuming the regular element abundances of the interstellar medium. It is given in units of 10^{22} atoms per cm^{-2}. However, interstellar medium does not only consist of hydrogen therefore other elements have to be taken into account such as iron and oxygen. We chose the variant **tbnew_feo** to model absorption since it also offers to vary the absorption columns of these two elements and considers the redshift of the observed source. In order to properly model the absorption the abundance of elements in the interstellar space is set to the values as described in the work of Wilms et al. (2000). In addition the cross sections tables as derived in the work of Verner et al. (1996) were used. The impact of this absorption model with different values of N_H on a simple powerlaw spectrum with $\Gamma = 2$ is shown in Fig. 3.9.

For further details about this model see the work of Wilms et al. (2000) or the homepage at Remeis-Observatory[4].

3.8 Overall Spectrum

Using the three models described above we are able to create a description of the expected spectrum of an AGN processed by the lamppost structure.

---

[4]http://pulsar.sternwarte.uni-erlangen.de/wilms/research/tbabs/

detconst refers to a constant applied to each observing instrument in order to correct for calibration issues. For further discussion see section 5.2.

relxill provides the incident powerlaw and relativistic reflections expected for an AGN. It is used in its lamppost version including the density parameter log(N) as a free value. The inner radius of the accretion disk R_{in} is intrinsically determined by the ISCO and therefore calculated by the spin parameter a of the black hole. R_{out} is fixed to the highest possible value of $400\,\mathrm{r}_g$. The redshift z has been looked up in the simbad database and is also assumed as fixed. Also the reflection fraction f_{refl} is intrinsically determined by the other parameters which should resemble the lamppost structure. Free parameters of the **relxill** model then are

- The normalization *norm*

- The lamppost height h in the units of r_{EH}

- The spin parameter a

- The inclination i

- The photon index Γ

- The ionization parameter in the form of $\log(\xi)$

- The iron abundance A_{Fe}

- The density parameter in the form of $\log(N)$

The xillver model is used in order to account for additional reflection components occurring not in the direct vicinity of the black hole where relativistic reflections are present but in regions of the accretion disk farther out. Due to lower photon energies of thermal radiation and the cross sections of a variety of elements, for example carbon, nitrogen and oxygen, being located at energies below $10\,\mathrm{keV}$ a significant amount of radiation is absorbed and re-emitted which results in absorption edges and additional emission lines (Matt et al., 1993). Using the xillver model in the version where it is only generating the additional reflection features but not the incident powerlaw which is already represented by the relxill model we can account for these additional features in the spectrum. The energy cutoff E_{cut} is set fixed to $300\,\mathrm{keV}$ and the material farther out in the disk is assumed to be neutral which means that $\log(\xi)$ is set to 1. Like in the relxill model the cosmological redshift can be looked up. The free parameters then are

- The normalization *norm*

- The photon index Γ

- The iron abundance A_{Fe}

- The inclination i

- The reflection fraction of the xillver model f_{refl}
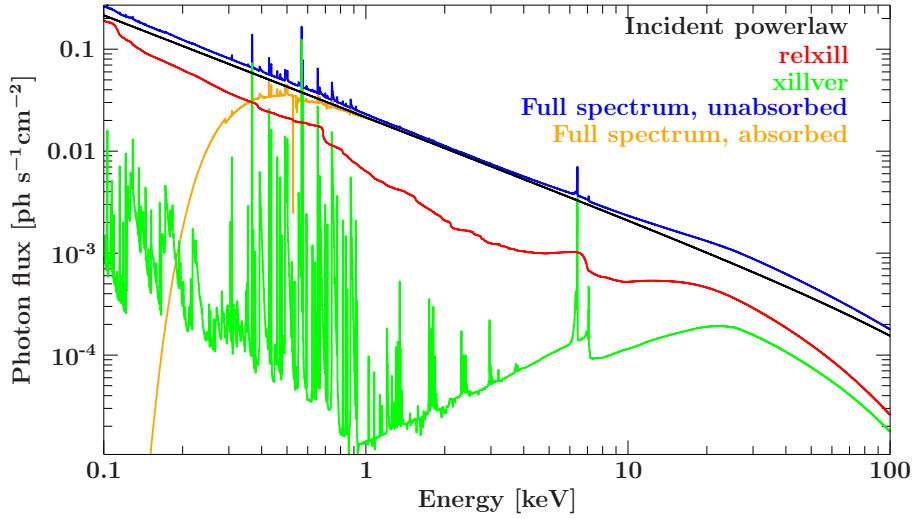
Figure 3.10: Decomposition of the expected spectral form consisting of the models described in this section.

N_H is a value which can be obtained using the HEASARC N_H-Tool (Kalberla et al., 2005; Dickey & Lockman, 1990).

The overall model then can be written as

$$F(E) = \mathrm{detconst} \cdot \mathrm{tbnew\_feo} \cdot (\mathrm{relxilllpD} + \mathrm{xillver})$$

Both of the reflection models in fact use some common parameters which are determined by the lamppost structure namely

- The photon index Γ

- The iron abundance A_Fe

- The inclination i

All these parameters are not treated for each model individually but assumed to be the same for each. This state of two parameters of different models treated the same is called parameter **tying**.

A decomposition of the expected spectrum and its components is shown in Fig. 3.10. Here f_refl is set to 0.3 for both reflection models, $\Gamma = 2$, the iron abundance A_Fe is 1, $\log(\xi)$ of the xillver model is assumed to be 1 which represents unionized material. The source is seen under an angle i of 30°, the black hole is maximally rotating with $a = 0.998$ and the primary X-ray source is located at $h = 6r_g$. Ionization of the relativistic reflecting material is set to an intermediate value of $\log(\xi) = 2.8$ and the density parameter is set to the lowest possible value of $\log(N) = 15$ which was also chosen as fixed in other models, in particular $\log(N) = 15$ and is fixed internally in the xillver model (García et al., 2013). The hydrogen column N_H of the absorbed spectrum is 0.05.

4 Numerical methods

The most popular method to find a parameter set of a model which fits a given dataset best is traditional χ^2-minimisation, also referred to as spectral fitting in context of spectroscopy. This topic is well covered for example in Bevington & Robinson (2003). This More complicated models with maybe even difficult numerical behaviour may provide multiple parameter combinations which according to the statistics describe the data in an acceptable way. Also fitting does not intrinsically provide information about the parameter space with respect to multiple possible solutions or parameter correlations. Already the first attempts to fit the data with the model described above lead to a variety of alternating results. Thus it is necessary to take the shape of the parameter space into account. In general we want to step back from the idea that there is one parameter combination describing the data best and focus on the probability distributions of these and their correlation. A very suitable way to derive this information is to apply **Monte Carlo** based methods which map the parameter space with respect to the probability of certain parameter sets. We focus on the affine-invariant ensemble sampler for Markov Chain Monte Carlo first implemented in Python by Daniel Foreman-Mackey, David W. Hogg, Dusting Lang and Jonathan Goodman as described in their paper (Foreman-Mackey et al., 2013). A port to S-Lang has been done by Michael A. Nowak (MIT) and is available in the Remeis-ISISscripts. The following considerations should give an overview of the technique applied to derive probability distributions, for a more detailed and theoretical view onto this topic see the paper proposing the Markov Chain Monte Carlo (**MCMC**) algorithm used here by Goodman & Weare (2010).

4.1 Markov Chain Monte Carlo

Markov property: The Markov property describes a process the future behaviour of which is not depending on its current state.
Markov Chain: A process satisfying the Markov property is called Markov Chain. In particular the term „chain" denotes the sequence of variables the process goes through, for example the time, or in this case, the number of iterations of a random walk. Following the review of Sharma (2017) on MCMC methods in general we want do develop a basic understanding of the way that is used to derive the probability density function (PDF) using statistical properties of Markov chains. A Markov chain is denoted by a sequence X_n, so the distribution can be written using the notation

$$\mathrm{Prob}(X_{n+1}|X_n)$$

by using the property that the distribution of X_{n+1} only depends on the distribution of X_n, which corresponds to the Markov property. The probability of a state change in a continuous parameter space during the next iteration can be written using the transition

probability function

$$K(x, y) = \text{Prob}(X_{n+1} = y | X_n = x)$$

whereas K takes the form of a matrix K_{xy} in a discrete parameter space and is also called **transition kernel**. If it is possible for a Markov Chain to step from a state x to a state y it is called **irreducible** which means that

$$\exists n \in \mathbb{N} \ : \ K_{xy}^n > 0$$

The Markov chain can also be irreducible and have a unique, stationary state which is called **positive recurrent**. Also the chain is considered aperiodic. Now take any initial parameter configuration denoted by a vector λ and apply the transition operator K many times then it will converge to its unique stationary state π:

$$\lim_{n \to \infty} \| \lambda K^n - \pi \| = 0$$

To actually compute the probability distributions of a function $g(x)$ on π one can make use of the fact that by applying the law of large numbers, the expectation value $E_\pi[g(x)]$ is represented by the average of the output of the Markov chain:

$$E_\pi[g(x)] = \int g(x)\pi(x)\mathrm{d}x = \lim_{n \to \infty} \frac{1}{n} \sum_{i=1}^{n} g(x_i)$$

A Markov chain with a stationary distribution can also be **reversible** with respect to time or iterations. If it satisfies this property it shows the same behaviour if started at the stationary distribution also if it is calculated in reverse:

$$\text{Prob}(X_{n+1}, X_n) = \text{Prob}(X_n, X_{n+1}) \Leftrightarrow \pi(X_n)K(X_n, X_{n+1}) = \pi(X_{n+1})K(K_{n+1}, K_+n)$$

This condition is also called **condition of detailed balance** and has not necessarily to be true for a Markov chain but if it is, the chain also has a stationary distribution and therefore this a strong condition used by a majority of sampling algorithms. The general goal is to find this stationary distribution as it represents the PDF for a parameter on a specific dataset.

4.2 The MCMC Hammer

The sampling algorithm used by the MCMC implementation in **emcee** (Foreman-Mackey et al., 2013) is mainly based on the **Metropolis-Hastings-algorithm**, a comparatively simple and widely used technique developed by Metropolis et al. (1953) and Hastings (1970).

Again, following the considerations of Sharma (2017) we propose a distribution $f(x_n)$ on a state space E whereas the initial state $x_n \in E$ is not depending on x_{n-1}. The mechanism to derive the next state consists of two steps. First a so called **proposal distribution** $q(y|x)$ has to be specified. To decide whether the new state can be accepted one can make

use of the acceptance ratio which can be defined as

$$\alpha(x,y) = \min\left(1 \ , \ \frac{f(y)q(x|y)}{f(x)q(y|x)}\right)$$

Note that for $f(y)q(x|y) < f(x)q(y|x)$ the acceptance ratio is always 1. The transition kernel K now takes the form of

$$K(x,y) = q(y|x)\alpha(x,y)$$

By comparing this after each evaluation to a newly drawn random variable $U \in [0,1]$ it can be decided whether the new state is accepted or not:

$$U < \frac{f(y)q(x_n|y)}{f(x_n)q(y|x_n)} \Rightarrow x_{n+1} = y$$

where the implication on the right side is meant as an assignment. The algorithm itself does not specify the actual form of the proposal distribution $q(y|x)$. There exist many possible ways to approach this problem. Foreman-Mackey et al. (2013) give a multidimensional Gaussian distribution which is centered around x_n as a common example.

4.3 Application to data

To use this sampling algorithm to obtain information about the PDF of parameters for a given dataset and model applied to it prior, a specified amount of **walkers** is distributed over a certain region in the parameter space in which the pdf is meant to be obtained. The term "walker" refers to one full set of parameters which is entered into the algorithm described above. The initial distribution can also either be of a Gaussian distribution around a certain parameter combination which is expected to be close to the actual best fit or randomly distributed over the region in which the PDF is supposed to be obtained. The walkers „walk" through the parameter space following the path which is generated by the stepping of the random walk of the algorithm. An example path for the parameter Γ of the relxilllpD-model is given in fig 4.1.

4.4 Software in use and computational effort

The evaluation of the relxilllpD and xillver models is comparatively expensive in terms of computing time. Due to the separate power law indices of XMM-Newton and NuSTAR both models were calculated double as much. Also the number of walkers per free parameter was chosen to 100 to gain a sufficient amount of significance. The Interactive Spectral Interpretation System (ISIS) developed by J.C. Houck and L. A. Denicola (see Houck & Denicola (2000) for detailed information or the homepage at http://space.mit.edu/asc/isis/) is very capable of analysing X-ray spectra and also offers a high programmability because it is based on the interpreted language S-Lang which makes it very suitable for this task. MCMC as described above was implemented in S-Lang and is available to the public in the Remeis ISISscripts at the homepage of the Remeis observatory Bamberg at http://www.sternwarte.uni-erlangen.de/isis/. In fact I spent a large amount of time on
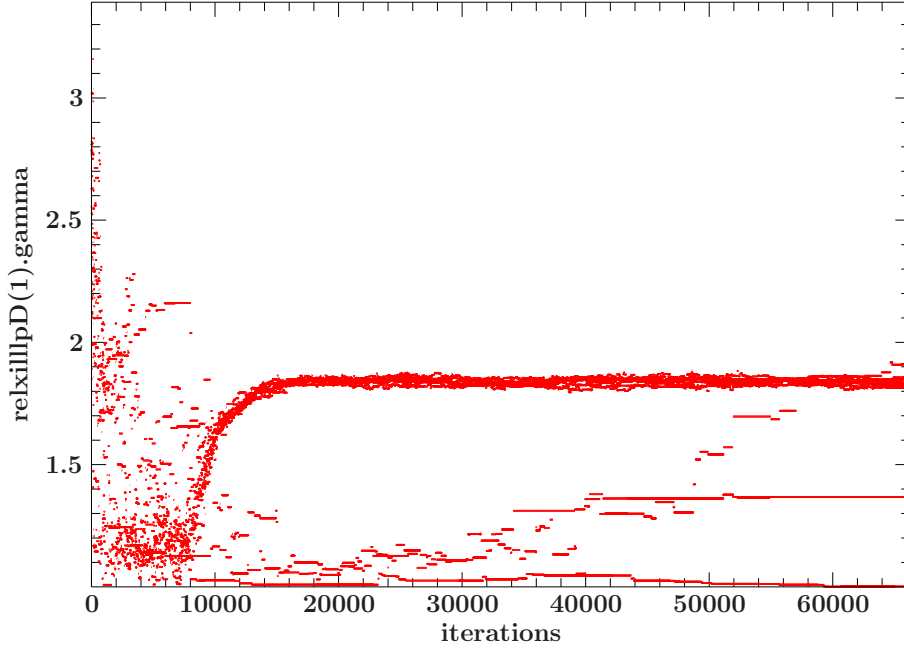
Figure 4.1: Example path of one walker for the Γ-parameter of the relxilllpD-model. Note
that for the beginning iterations the walker changes it's position rather drasti-
cally but starts to settle down in a region about $\Gamma = 1.8$ which in the end also
turns out to be the most probable value. During the whole run it occasionally
jumps to lower values for certain steps

correcting some bugs in the mentioned MCMC implementation and adding features which
make it possible to reliably use the sampling algorithm and process the large Markov
chains in the first place. By taking into account that the model had 12 free parameters
each, xillver and relxilllpD, were calculated 2400 times for each iteration. Taking into
account the last iteration number of 76250 the total number of evaluations is 183 million.
To speed up the computation time we made use of the integrated **MPI** (Message Pass-
ing Interface) function of the emcee implementation in ISIS and distributed the task over
multiple hosts which communicated over ethernet. The overall time used on all cores was
to 1651 h.

4.5 Determination of probability density

To judge whether a MCMC run converges to an acceptable set of parameters one can use
the **acceptance fraction** a_f. It is determined for each iteration by the number of walkers
n_a which did an acceptable step against the total number of walkers n_w:

$$a_f = \frac{n_a}{n_w}$$

According to Foreman-Mackey et al. (2013) there is no full conclusion about which value of
the acceptance fraction represents a convergence of the sample. However, $a_f \sim 1$ implies

that almost all walkers did an acceptable step and the complete chain does a random walk. This of course does not reflect the actual data. In contrast for $a_f \sim 0$ the majority of steps is rejected and the chain has nearly no independent samples which does not represent the target density.

Foreman-Mackey et al. (2013) suggest that is acceptable if $a_f \in [0.2, 0.5]$ which is also supported by Gelman et al. (1996) and we choose to agree with. Because it is a non-trivial problem the topic is undergoing quite extensive discussions, see for example Cowles & Carlin (1996) for a detailed review of this topic. The sampling then has converged at the point where the acceptance fraction does not change any more. Integrating over the iterations of all walkers from this point on gives the probability distribution function. The integral over the probability space is called **cumulative sum** (CSum) and is 0 at the lower limit of each parameters probability, 1 at the upper limit and monotonically increasing. Rapid changes in the cumulative sum indicate high probability.

5 X-ray Observations

X-ray radiation can not penetrate the earths atmosphere. Therefore observations of these kind of emission can only be carried out in space by special telescopes.

5.1 X-ray telescopes

5.1.1 Optics

Conventional optical telescopes make use of mirrors to influence the path of light in order to focus the incident radiation onto the focal plane. This is possible because radiation of the optical spectrum is reflected by a clean surface in the first place. X-rays in contrast would penetrate a mirror and be lost. Fortunately the reflection of radiation depends on the incident angle. According to Krauss (2016) the critical angle of incident θ_c can be given as

$$\theta_c = 5.6' \sqrt{\frac{\rho}{1\,\mathrm{g\,cm^{-3}}}} \frac{\lambda}{1\,\mathrm{nm}}$$

which is in general below $1°$ for radiation in this energy regime and makes a construction like optical telescopes impractical to observe X-ray emission. Wolter (1952) addressed this problem, when he wanted to build an X-ray microscope, by using a cylindrical shaped mirror of slight parabolic form of which X-rays are reflected under a very small angle onto the focal plane which is located comparatively far behind the mirror itself. Later it was also possible to add an additional layer of reflection behind the parabolic cylinder consisting of a similar construction with hyperbolic shape. By doing so the focal length could be decreased. For better effective area many of theses shells are nested. The schematic setup of this kind of optics can be seen in Fig. 5.1, Fig. 5.3[1] shows the mirror shells of XMM on earth. At the end of the path of rays there is a detector in general consisting of a CCD-chip which can not only obtain spatial resolution but also can do spectroscopy by measuring the energy deposition of individual photons by measuring the amount of electrons which are dissociated due to the impact.

5.1.2 XMM-Newton

XMM-Newton is the current flagship spacecraft of the European Space Agency. It is an X-ray observing satellite which was launched in December 1999 into an orbit with a perigee of $5660\,\mathrm{km}$ and an Apogee of $113\,000\,\mathrm{km}$ on which it orbits earth in a period of $48\,\mathrm{h}$. The focal length is $7.4\,\mathrm{m}$ at a mass of $3800\,\mathrm{kg}$. It can observe X-ray emission in the energy range of $0.15\,\mathrm{keV}$ to $12\,\mathrm{keV}$ at a spectral resolution of the main instrument,

---

[1]Image source: https://heasarc.gsfc.nasa.gov/docs/xmm/xmmhp_gal_hard_photo_mir.html
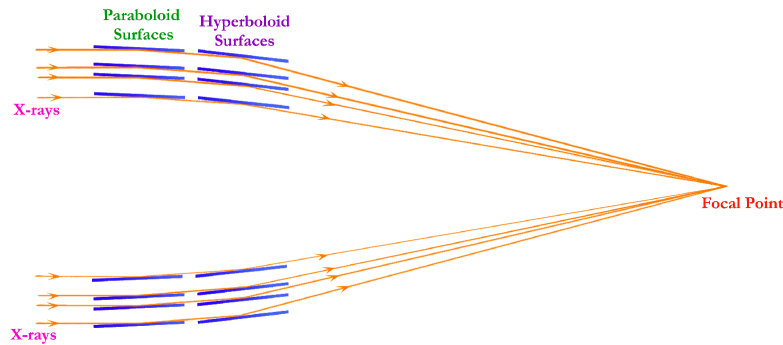
Figure 5.1: General setup of a Wolter telescope with path of rays (Taken from Gorenstein, 2012)
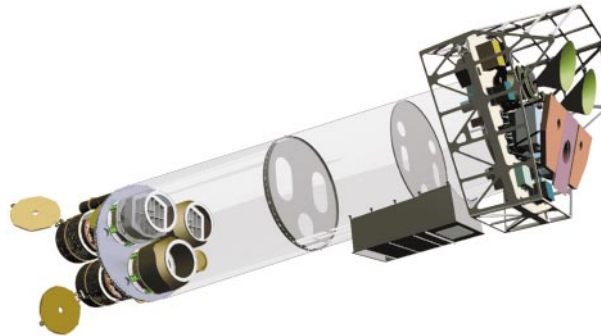
Figure 5.2: Sketch of the *XMM-Newton* satellite. (Taken from Jansen et al., 2001, modified)

called **Epic-PN**, of 150 eV. To gather more effective area *XMM-Newton* uses three Wolter telescopes in the same orientation for observations. (Jansen et al., 2001)

5.1.3 NuSTAR

NuSTAR is an X-ray observing satellite developed and built by **NASA** and launched into an orbit of Peri-/Apogee of 610 km / 650 km in June 2012. The orbital period is 1.6 hour due to the comparatively low height. With a mass of 350 kg it is only a fraction of the mass of *XMM-Newton*, because unlike XMM it's region between the mirror shells and the focal plane does not consist of solid material but is a construction of a deployable mast. Therefore the focal length could be increased to 11 m. It covers a spectral range from 3 keV up to 79 keV which is known as the hard X-ray regime and makes a higher focal length necessary due to the lower incident angle of photons on the mirror shells. *NuSTAR* makes use of two CCD chips in order to obtain an energy resolved spectrum. The corresponding instruments are called **FPMA** and **FPMB** respectively. The spectral resolution lies in the range of 400 eV - 900 eV. (Harrison et al., 2013)
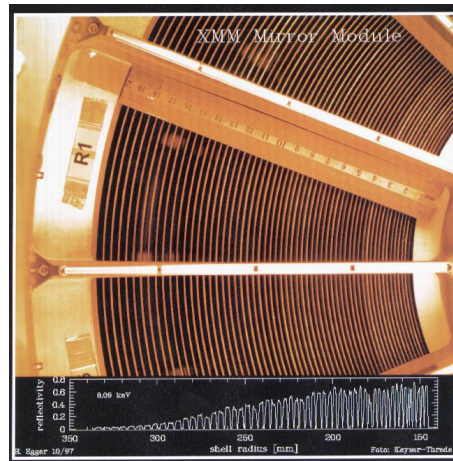
Figure 5.3: The mirror shells of *XMM-Newton* (Image courtesy of the Max Planck Institute for Extraterrestrial Physics, 1998 calendar picture, taken from NASA)
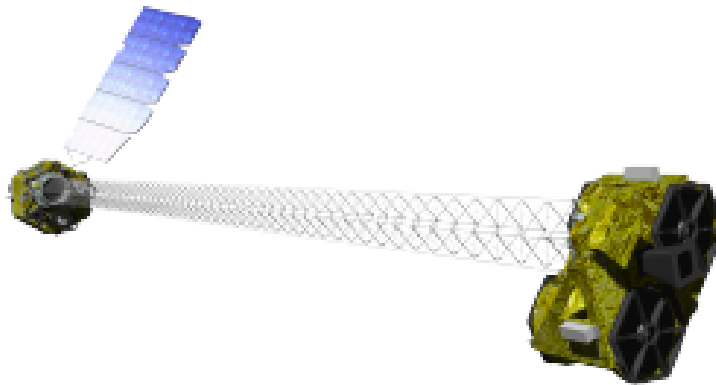
Figure 5.4: Sketch of the *NuSTAR* satellite. (Taken from Harrison et al., 2013, modified)

5.2 Obtaining spectra

The continuous flux of an X-ray source in the sky is not the only component which is source of radiation measured by the detector. There is also a constant background signal arising from

1. Thermal and intrinsic fluctuation of the detector

2. Background radiation by high energetic particles and cosmic rays

To distinguish real signal of the source from this background signal it is necessary to extract it and determine the background spectrum and its contribution. To do so one can select a region next to the sources emission region on the detector where no radiation of the main source had impact. The spectrum in this region is then subtracted from the overall spectrum measured at the sources position and weighted with the corresponding

area. In addition to each dataset provided by an instrument an empirical constat called **detconst** is applied which can correct for normalization issues due to detector calibration. For a more detailed description of spectrum extraction and also detector specific effects in general see Fink (2016).

The sources spectra used in this work consist of one example of a sample of 25 AGN observed with *XMM-Newton* and *NuSTAR*, liberally provided by Marco Fink who extracted these by also taking into account variability in terms of time dependence and hardness ratios to be able to focus on a more stable spectral shape. For a detailed explanation of this procedure see Fink (2016), especially chapter 4, X-ray Data Analysis, and chapter 5, Extraction and model details.

5.3 Cross calibration

In general the spectrum measured in the low energy range by *XMM-Newton* should continue with the same spectral properties in the higher energy regime disregarding the normalization due to different detector efficiencies and effective areas. This is especially true for the slope of the powerlaw, namely the parameter Γ in the models applied. However, there is evidence that this is not true. In figure 5.5 are shown several photon indices determined for 10 sources by Gokus (2017). It is clearly visible that Γ determined with the data of *NuSTAR* tends to be systematically higher than determined by *XMM-Newton* data which corresponds to a steeper powerlaw slope. The same was also found for the sample analyzed by Fink (2016). To address this problem we will fit two separate powerlaw indices to the data and also determine if the same property is present when not fitted with the classical χ^2-minimization method.
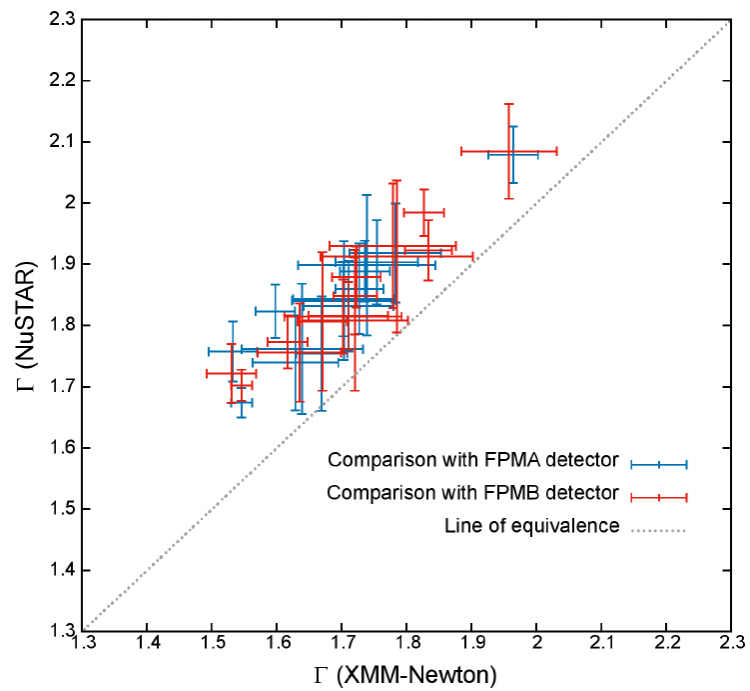
Figure 5.5: Correlation between photon indices determined by *XMM-Newton* and *NuS-TAR*. The photon indices obtained with *NuSTAR* data are systematically higher than the one by *XMM-Newton*. (Taken from Gokus, 2017)

6 Arakelian 120

6.1 Characteristics

Arakelian 120 (Ark120) (see Fig. 6.1[1]) is a comparatively luminous Seyfert I galaxy located in the constellation of orion at coordinates $\alpha_{\text{J2000.0}}$ $05^{\text{h}}16^{\text{m}}11.395^{\text{s}}$ $\delta_{\text{J2000.0}}$ $-00°08'59.65''$[2]. The mass of the black hole in the center is estimated to $1.50(19) \times 10^8 \text{M}_\odot$ (Wandel et al., 1999). With the bolometric intensity of $L \sim 10^{45}\text{ergs}^{-1}$ of the core (Vaughan et al., 2004) the luminosity is at $\sim 5\,\%$ of L_{Edd}. Ark120 is known to be radio quiet AGN but also shows some radio emission (Ho, 2002). The hosting galaxy is of type S0/a and seen under an inclination of $i \sim 26°$ (Nordgren et al., 1995) and does not cause any additional amount of absorption in the spectrum therefore it is also called a **bare** AGN (Ward et al., 1987). In fact it is stated by Porquet et al. (2017) that this AGN is indeed the „brightest and cleanest bare AGN known so far". This is also why we focus on this source.

---

[1]Image source: http://www.astro.gsu.edu/AGNmass/details.php?varname=6
[2]from the simbad database: http://simbad.u-strasbg.fr/simbad/sim-id?Ident=Ark+120
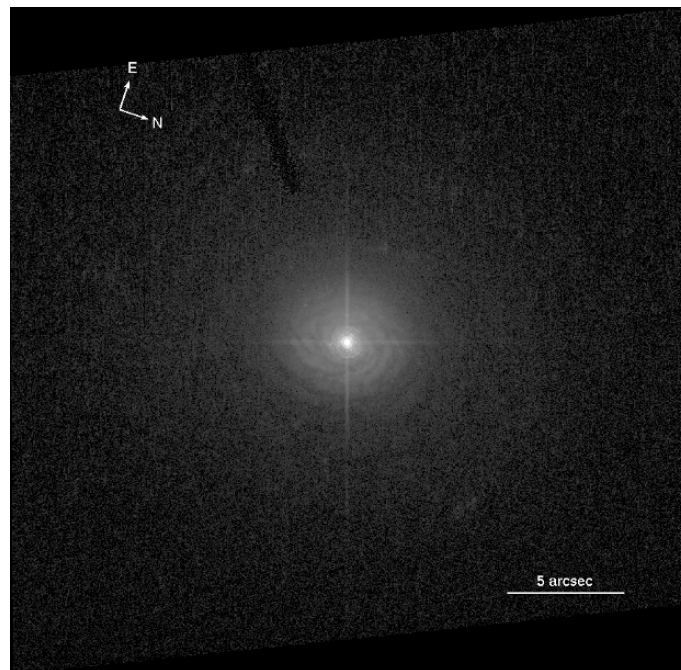
Figure 6.1: Image of Ark 120, captured with the Hubble Space Telescope in the infrared using the ACS instrument in combination with the F550M filter. (Image taken from The AGN Black Hole Mass Database)

Observatory	Observation-ID	Start	Exposure
XMM-Newton	0693781501	13-02-18 11:39	130 ks
NuSTAR	60001044002	13-02-18 10:46	55.3 ks

Table 6.1: Observations of Ark120 carried out by XMM-Newton and NuStar. (Data taken from Fink, 2016)
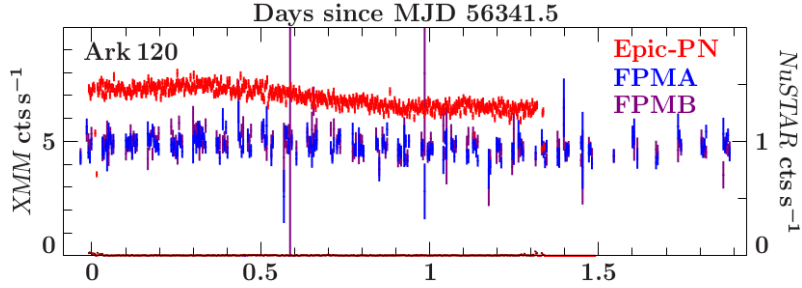
Figure 6.2: Lightcurve of Ark120 during the observations taken by the three instruments as labeled. (Taken from Fink, 2016)

Vaughan et al. (2004) report the presence of a broad iron Kα line complex which is larger then expected by assuming a source following the unified model. Thus more complicated spectral features like relativistic reflections or additional comptonisation is suggested (Porquet et al., 2017).

6.2 Observations and Extraction

As explained in section 5, X-ray observatories cover different energy ranges. In order to derive information about all spectral regions of interest it makes sense to use multiple instruments in different wavelength bands simultaneously. Ark120 was observed with the Epic-PN detector of *XMM-Newton* and the FPMA- and FPMB-detectors of *NuSTAR* in this manner. The combined energy range of these instruments is $0.15\,\text{keV} - 79\,\text{keV}$ which makes it possible to constrain the continuum emission and the iron line complex especially with the high spectral resolution of the Epic-PN detector of $150\,\text{eV}$. Information about the time of observation and exposure is given in tab. 6.1. Extraction of the spectral data has been done by Fink (2016), see this work for more details regarding this aspect.

7 Results

7.1 Spectral Fitting

Figure 7.1 shows the extracted spectrum fitted with a simple powerlaw and galactic foreground absorption leading to a photon index of $\Gamma = 1.92$. N_H is always set to 0.0978 as it is determined by HEASARC N_H-Tool, the same is true for the cosmological redshift z which is extracted as 0.0323 from the simbad database. The residuals make the iron $K\alpha$ line complex visible and show that the continuum emission is not accurately described by a simple powerlaw. To explain these features we made use of the model combination explained in section 3.8.

Fig. 7.2 shows the result of the best fit. According to the reduced χ^2 of 2.09 the model is not entirely capable of describing the given dataset. However, it suggests a central black hole spinning close to its theoretical maximum, see $a \sim 0.959$. Interestingly the photonindices Γ_2 and Γ_1 for *XMM-Newton* and *NuSTAR* only vary by $\sim 0.002\,78\,\%$ which is not in agreement with Gokus (2017) and Fink (2016). The height h of the source is with $\sim 4.89\,r_\mathrm{EH}$ reasonable low and can account for relativistic features in the spectrum. Fink (2016) found it with the relxill-lamppost model without varying density to be at $3.36\,r_\mathrm{EH}$. This additional parameter can be determined to $\log(N) = 15.70$ which is higher than $\log(N) = 15$ as assumed by the former lamppost model. The higher height of our fit could be accounted for this additional component which can compensate for the need of a
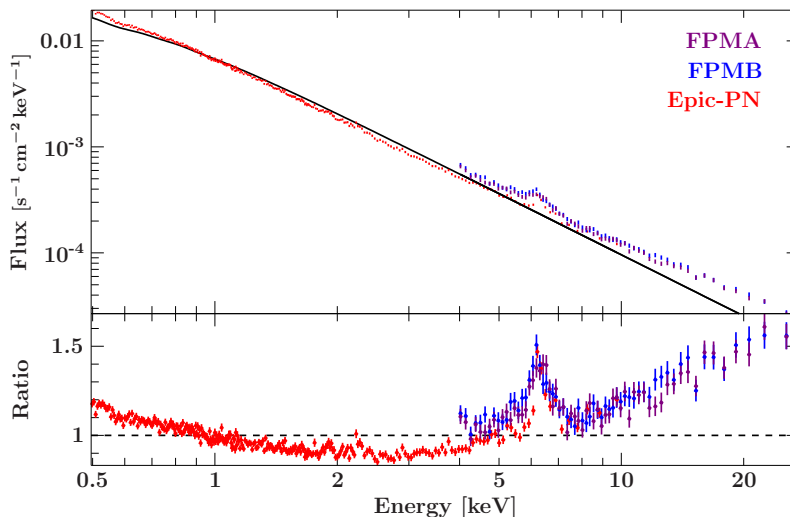
Figure 7.1: Spectrum of Ark120 with a simple powerlaw fit and galactic absorption, $\Gamma = 1.92$, $N_\mathrm{H} = 0.0978$. The iron $K\alpha$ line complex is clearly visible. Also the continuum is not properly described.
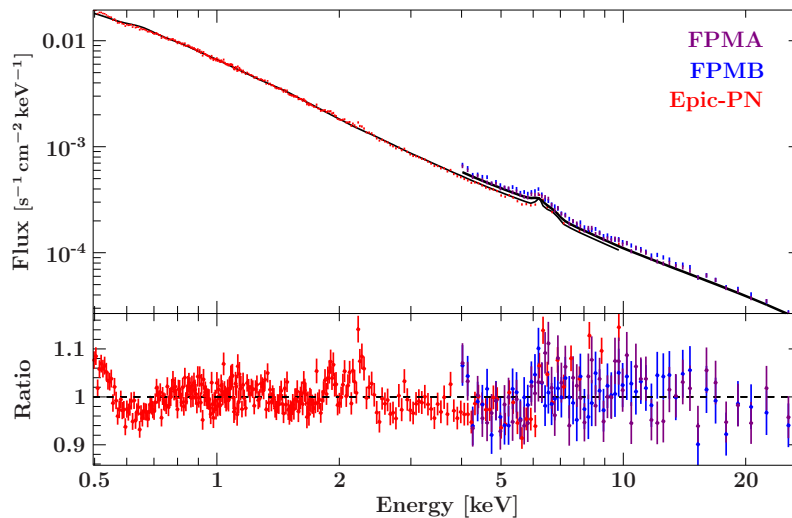
Figure 7.2: Spectrum of Ark120 fitted by the assumed model, parameters given in tab. 7.1

Parameter	value
h	4.87 r_{EH}
a	0.9587
i	$37.979\,85°$
Γ_1	1.839
Γ_2	1.839
$\log(\xi)$	2.77
A_{Fe}	3.296 $A_{\mathrm{Fe}\odot}$
$\log(N)$	15.70
f_{refl}	2.726e-05
χ^2_{red}	2.09

Table 7.1: Parameters for the best fit as seen in Fig. 7.2

primary X-ray source sitting closer to the event horizon. As determined by Fink (2016), the inclination i between the observer and the accretion disk is 40.1° which is in good agreement with $i \sim 38.0°$ found by our fits.

7.2 MCMC results

Traditional spectral fitting can only determine one set of parameters which supposedly fits the data best. Markov Chain Monte Carlo analysis in contrast can give the probability distribution over a given interval.
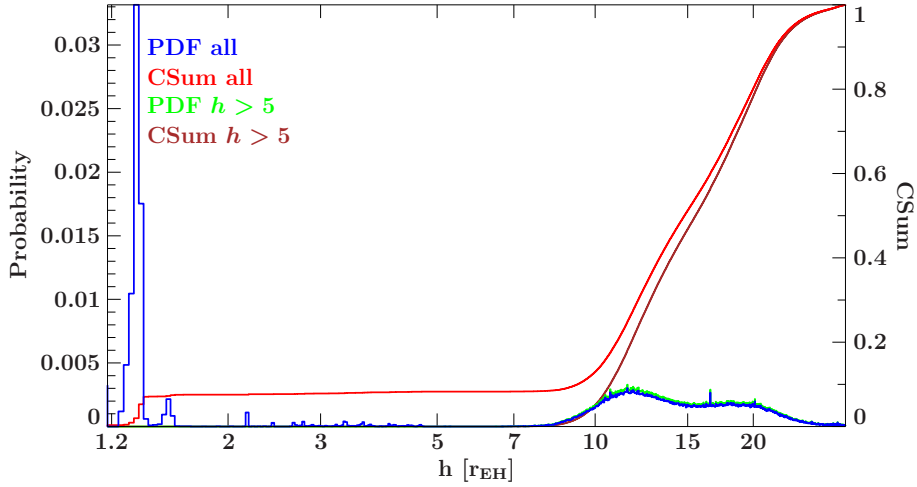
Figure 7.3: Probability distribution function and cumulative sum for the lamppost height h. Blue: PDF of all walker; Green: PDF for $h > 5r_{\mathrm{EH}}$; X-axis is logarithmic

7.2.1 Single Parameter Probability Distributions

Lamppost height

The first interesting thing to note is the height h of the lamppost source. Fig. 7.3 shows the probability distribution function for this parameter. Plotting the distribution in a coordinate system with a logarithmic x-axis makes two possible solutions visible. First there is a region with $8r_{\mathrm{EH}} \leq h \leq 30r_{\mathrm{EH}}$ which covers a broad interval with the probability $P(8r_{\mathrm{EH}} \leq h \leq 30r_{\mathrm{EH}}) \sim 7\,\%$. $90\,\%$ of the probability space for h is covered in this region. But there is also a sharp peak visible at $h \sim 1.3r_{\mathrm{EH}}$ which covers $\sim 10\,\%$ of the probability space for h. Both are possible solutions of the model fitting the data with respect to h and will be treated separately in the following. Hence the green distribution in the diagram represents the probability distribution for the solution with $h > 5r_{\mathrm{EH}}$ (solution 1) and the purple one (solution 2) for $h \leq 5r_{\mathrm{EH}}$. Only about $10\,\%$ of the walkers settled down in the second solution so the noise is expected to be a factor 10 higher. The height for solution 2 is similar to $h = 1.124r_{\mathrm{EH}}$ which is what Fink (2016) found for a relxill flavour without addition density parameter, in fact it is a bit lower which is in agreement with the fact that the density is lower in this model. In general a lamppost height as close to the event horizon as $h < 2$ is difficult to realize.

Detector constants

The offset constant for the *Epic-PN* detector of *XMM-Newton* is always assumed to be 1, the constants of *FPMA* and *FPMB* are relative to this. In Fig. 7.4 the PDF for the two detector constants is shown. Interestingly solution 1 gives for FPMA a Gaussian distribution centered around 1.11225 whereas the maximum of solution 2 is at 1.1529. This already indicates a correlation between h and the detector constants. For FPMB the behaviour is similar, the maximum for solution 1 is at 1.13576, for solution 2 at 1.19491 but the distribution does not show a bump as significant as for FPMA. It possible that the higher constant for the second solution is arising from the cross calibration issue
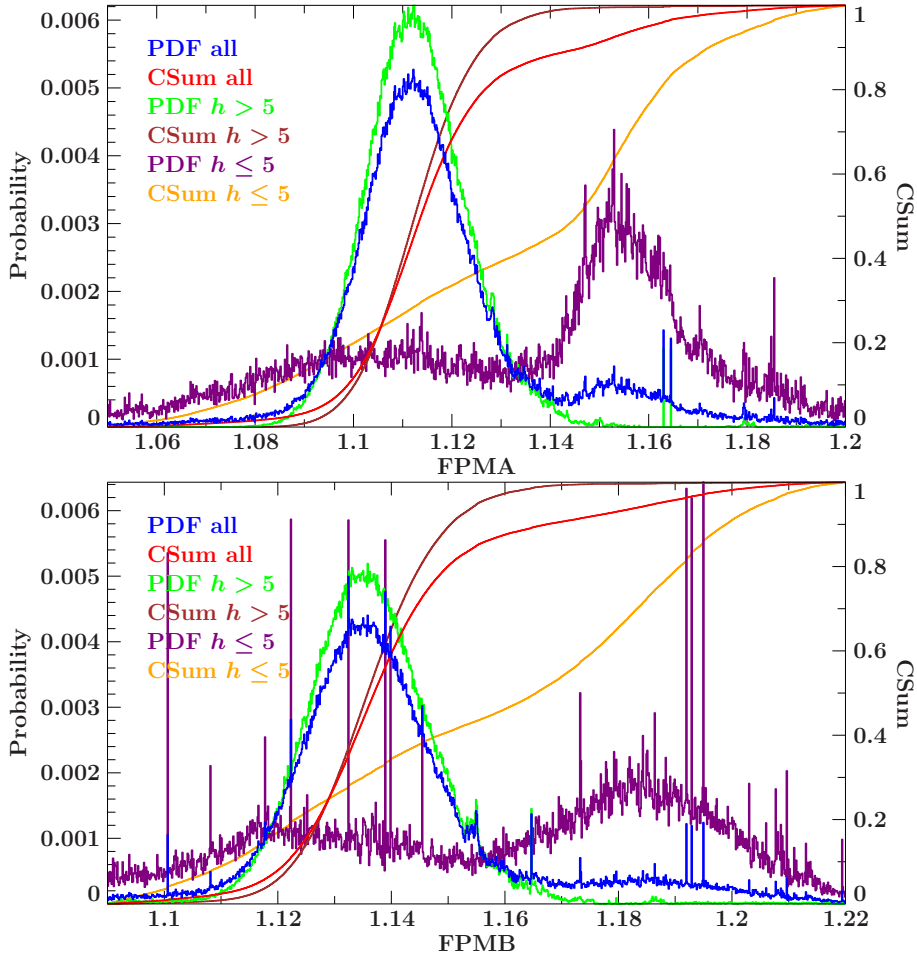
Figure 7.4: Probability distribution for the detector constants of the *FPMA* (top) and *FPMB* (bottom) instrument of *NuSTAR*.

explained in section 5.3. The comparison between the constants for both detectors yields to $FPMB = 97.93\,\%\,FPMA$ for solution 1 and $FPMB = 96.48\,\%\,FPMA$ for solution 2, indicating that FPMB is marginally more sensitive than FPMA. Also the distribution for the second solution is affected by more noise which is expected because only $\sim 10\,\%$ of the walkers can be used to determine the PDF. However, the PDF for the second solution FPMB in Fig. 7.4 shows some outstanding spikes whereas the PDF for the first solution is not affected by this kind of feature. The reason for that might be a numerical instability towards lower lamppost heights h.

Photon indices

Due to cross calibration problems explained in section 5.3 it is necessary apply separate continuum models to the *XMM-Newton* and *NuSTAR* data. Fig. 7.5 shows the determined probability distributions for the photon indices of the incident powerlaw, Γ_2 corresponds to the *XMM-Newton* data, Γ_1 to the *NuSTAR* data. The best fit as described in section 7.1, tab. 7.1 already shows that the two photon indices are very similar. Interestingly the PDF
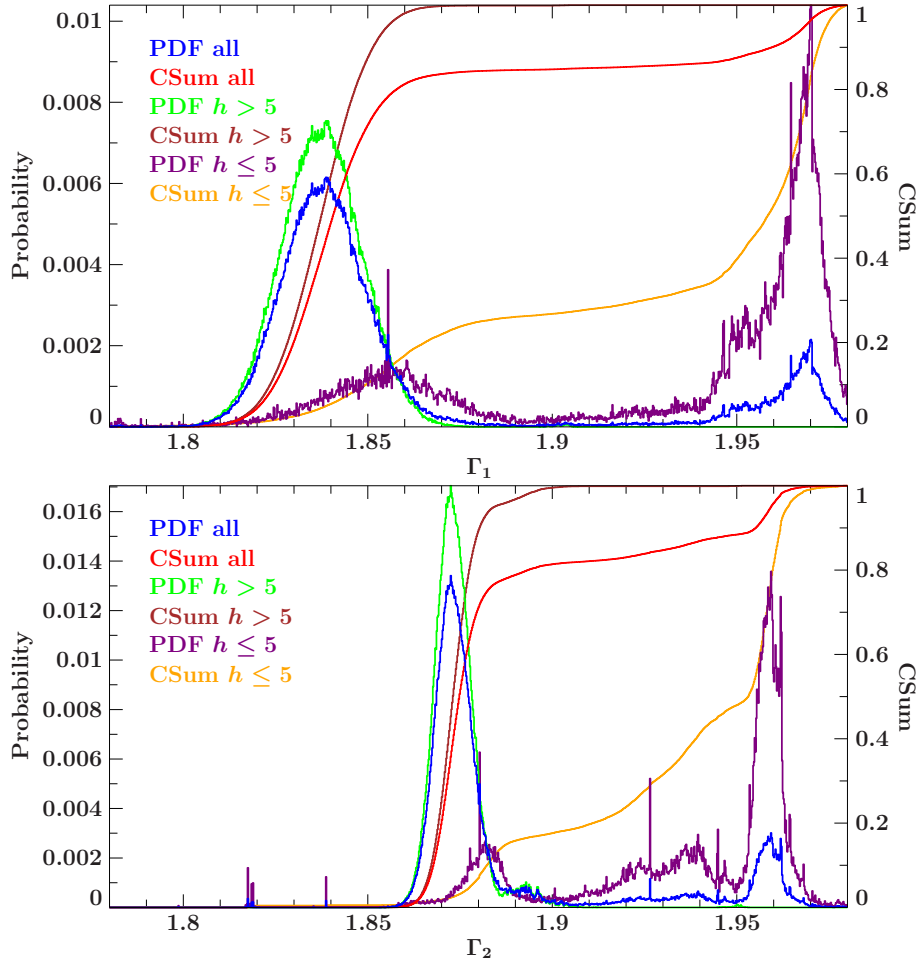
Figure 7.5: Probability distributions of the photon index for Γ_1 (*NuSTAR*) and Γ_2 *XMM-Newton*

of both solutions with respect to the lamppost height h have a maximum at very different values. Determination of the value for $\Gamma_{1,2}$ with highest probability leads to $\Gamma_1 = 1.8386$ and $\Gamma_2 = 1.8724$ for the distribution with larger lamppost height and $\Gamma_1 = 1.9700$ and $\Gamma_2 = 1.9592$ for the distribution with lower h. As can be seen from these values the photon index for *XMM-Newton* tends be higher than the value for *NuSTAR*. In addition the ratio Γ_1/Γ_2 is 0.9819 for solution 1 and 1.0055 for solution 2. Fink (2016) found $\Gamma_1 = 1.80(2)$ and $\Gamma_2 = 1.70(2)$ leading to $\Gamma_1/\Gamma_2 = 1.0588$. This is not in agreement with the photon indices obtained in this work. The probability distribution does not cover the values of the work by Fink (2016). Also the ratio is lower than 1 instead of higher which indicates that the cross calibration problem for *XMM-Newton* and *NuSTAR* for solution 1 leads to a marginally steeper powerlaw for *XMM*. Considering the probability densities for the two different photon indices there can be seen an overlap in the region of $1.85 \leq \Gamma \leq 1.86$ where both photon indices are in agreement with each other by the statistical value of 2σ deviation around their mean values. Additionally the difference between Γ_1 and Γ_2 is only 1.81 % for solution 1 and 0.45 % for solution two. This is significantly lower than 5.88 %
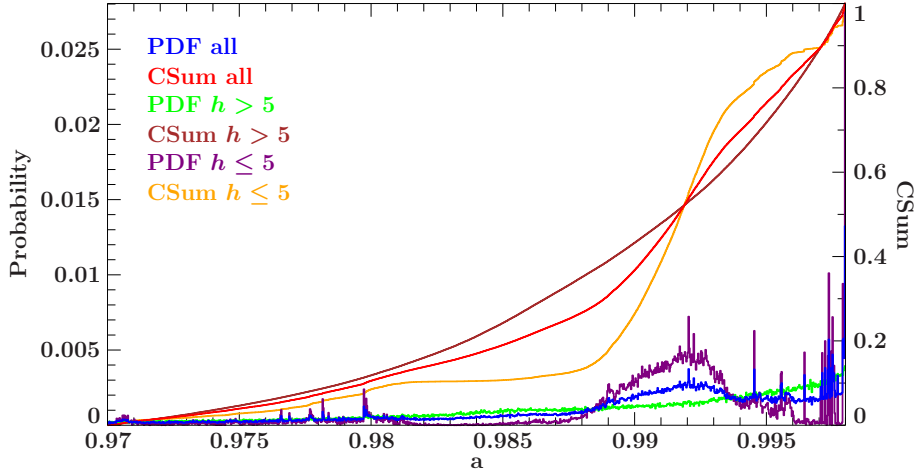
Figure 7.6: Probability distribution for the black hole spin a

as found by Fink (2016).

Black Hole Spin

The probability distribution for the black hole spin parameter is shown in figure 7.6. I can be seen that solution 1 tends to converge towards the theoretical upper limit of $a_{\mathrm{max}} = 0.998$. The cumulative sum for solution 1 therefore has a steeper increase towards a_{max}. Solution 2 has an extended region of high probability at $0.988 \leq a \leq 0.996$ which is also indicated by the higher slope of the cumulative sum in this region. Fink (2016) found a to be $0.994^{+0.003}_{-0.004}$ which lies well in this region. But by taking into account that the significance for solution 2 is only $11.11\,\%$ that of solution 1 it can be said that $a > 0.989$ with confidence of 1σ.

Density parameter

The density parameter $\log(N)$ is of special interest because the model used is the first one to be able to take the density of the accretion disk into account. The probability distribution is shown in Fig. 7.7 and suspects that both solutions have a clear maximum at $\log(N) = 16.12$. Solution 2 has tow side maxima, one at $\log(N) \sim 15.7$ and one at $\log(N) \sim 15.95$. Solution 2 also shows single spikes in the distribution, similar to what can be observed for the detector constants in Fig. 7.4. Since this solution corresponds to $h \sim 1.3 r_{\mathrm{EH}}$ which is very close to the event horizon of the black hole numerical instabilities could account for this problem. The determination of $\log(N)$ leads to the result that the density n of the accretion disk indeed is not equal to $10^{15} \mathrm{cm}^{-3}$ but more than a magnitude higher.

Inclination

The probability distribution for the inclination i, as seen in Fig. 7.8, is clearly centered around $64°$ for solution 1 and around $60°$ for solution 2. Again some spikes are visible in the distribution of solution 2. The result does not confirm the parameters determined by
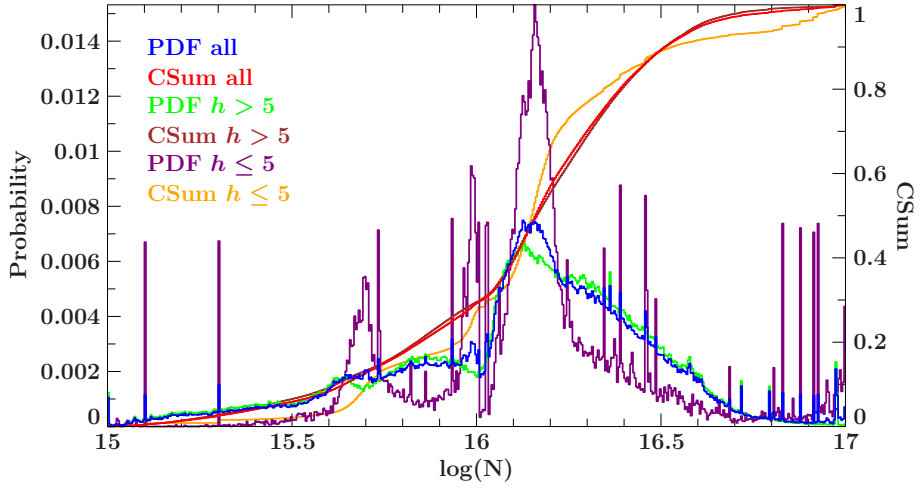
Figure 7.7: Probability distribution for the density parameter $\log(N)$
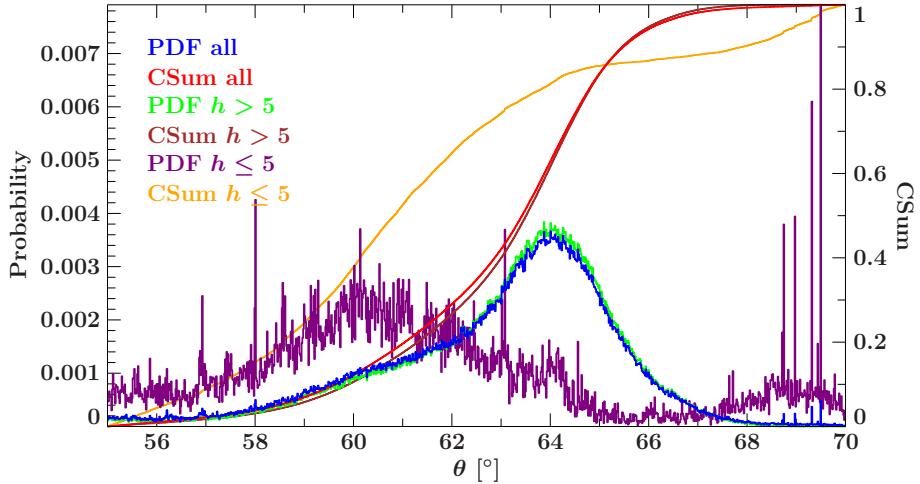
Figure 7.8: Probability distribution for the inclination i

Fink (2016) which is $40.1°$. However, the regions for both solutions are spread over $\sim 4°$ each which also does not include the parameters determined by Fink (2016). A possible explanation is the inclusion of a different density which may cause the inclination to get to higher values.

Iron Abundance

Tho iron abundance A_{Fe}, as shown in Fig. 7.9, is centered around $A_{\mathrm{Fe}} \sim 2.6A_{\mathrm{Fe\odot}}$ for both solutions. The distribution of solution 2 shows very high noise and no clear Gaussian distribution with a single maximum. Thus it is not possible to constrain a single value for A_{Fe} in the second solution. Fink (2016) obtained A_{Fe} to be $2.95A_{\mathrm{Fe\odot}}$ which lies in the region where solution 2 is considerable but outside of solution 1.
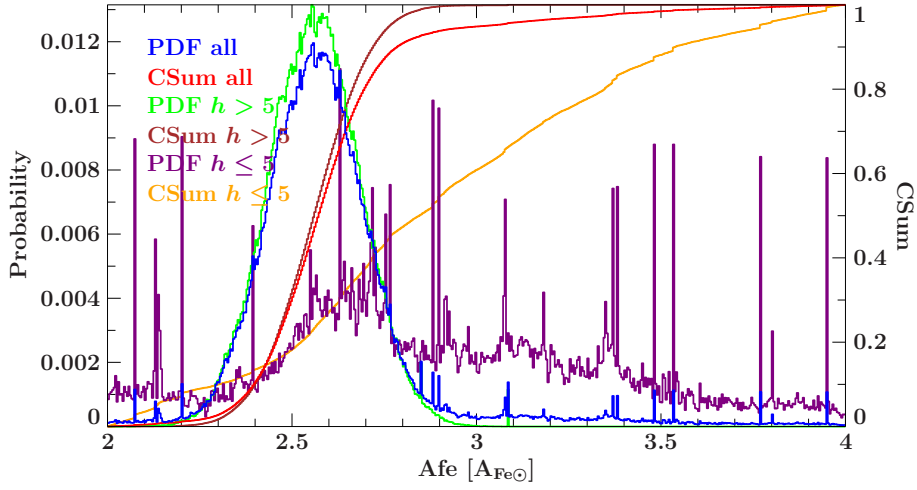
Figure 7.9: Probability distribution for the iron abundance A_{Fe}
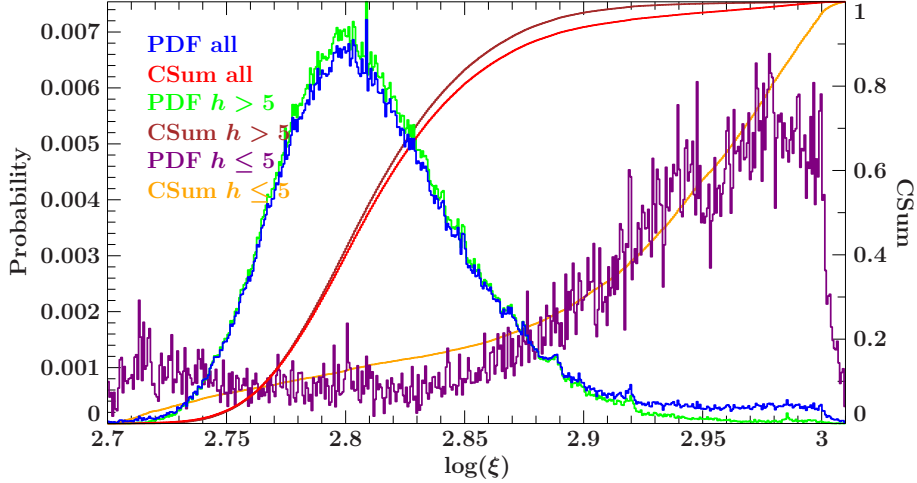
Figure 7.10: Probability distribution for the ionization state $\log(\xi)$

Ionization state

From Fig. 7.10 it can be seen that the two solution lead to different values for the ionization state. $\log(\xi)$ can be determined in the interval of $2.7 < \log(\xi) < 3.0$ for both possible solutions but maxima are at $\log(\xi) = 2.8$ and $\log(\xi) = 2.98$ respectively. The ionization state is expected do behave differently for different lamppost heights h, in fact if the source is closer to the accretion disk the ionization state should be fairly higher which is represented in the obtained probability distribution. Fink (2016) found this parameter to be 2.75 which lies in the range of possibility from the distribution obtained here.

Reflection fraction

The probability distribution for the amount of radiation reflected off the accretion disk, represented by f_{refl}, is shown in Fig. 7.11. Solution 1 clearly converges against the upper
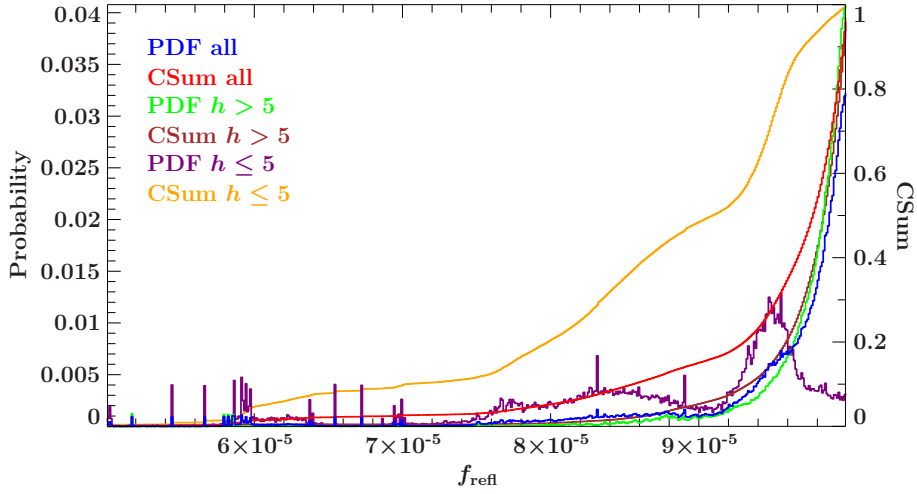
Figure 7.11: Probability distribution for the reflection fraction f_{refl}
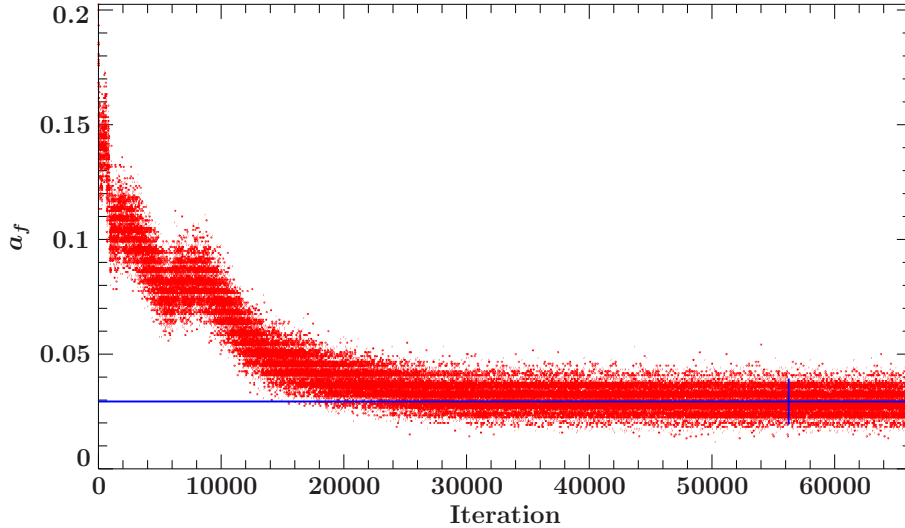
Figure 7.12: Acceptance fraction a_f for the Markov chain with respect to the number of passed iterations. The blue horizontal line represents the mean value of $\overline{a_f} = 0.029371$ over the last 10000 iterations, denoted by the blue vertical line

limit chosen for this parameter of 10^{-4}. Solution 2 in contrast has one local maximum at $f_{\mathrm{refl}} = 9.56 \times 10^{-5}$. A lamppost source at lower height h can intrinsically account for a higher amount of relativistic features in the spectrum. Therefore the reflection fraction can be lower as seen in solution 2.

7.2.2 Acceptance fraction

As explained in section 4.5 the acceptance fraction can be used to judge if a Markov chain converging to a specific set of parameters describes the data accurately. If so the acceptance fraction a_f is expected be higher than 0.2 but lower than 0.5. The acceptance

fraction of the Markov chain obtained by application to this data converges towards the mean value of $\overline{a_f} = 0.029371$ of the last 10000 iterations. This is not sufficient enough to be considered as describing the data accurately. Low acceptance rate can be caused by a long autocorrelation time, the time which is necessary to produce a reasonable sampling of the parameter space (Foreman-Mackey et al., 2013). But since the walkers did converge into specific parameter distribution (see Fig. 4.1) and the acceptance fraction is constant over a large fraction of iterations it is very likely that the probability distributions obtained in this analysis are the final ones.

7.2.3 Parameter correlations

Relativistic reflection models are comparatively complicated which often leads to correlations of different parameters. The Markov chain Monte Carlo method has the advantage of mapping the whole parameter space while sampling the data. Thus error contours are generated intrinsically and can easily be computed. As frequently mentioned in section 7.2.1 about single parameter probability distributions there are spikes present in the distributions, maybe due to numerical instabilities. To filter these out regions where the probability density behaves Gaussian were selected. All values above the local maximum generated by this Gaussian distribution are considered a spike and marked as a red pixel in the contour plots. Because there are two possible solutions present we show for each parameter of interest the contour plot of all walkers combined and for the more significant solution 1 in each figure. Also the plots have contours as levels drawn into the diagrams. Color and level correspond as

- Purple: $1\sigma \sim 68\,\%$

- Pink: $2\sigma \sim 90\,\%$

- Orange: $3\sigma \sim 99\,\%$

and the orange cross marks the combination of the most significant value. Because of the way the models treat some of the parameters the reflection fraction f_{refl} and the lamppost height h are inverted in the confidence maps.

Lamppost height h and norm of relxill

As can be seen from Fig. 7.13 the normalization of the relxill model and the lamppost height h are clearly correlated and even show two island of probability higher than $99\,\%$. The lamppost height h is negative in this plot because the model internally treats negative values of h as units if r_{EH} whereas positive values are expressed in units of r_{g}. The closer the primary X-ray source sits to the accretion disk the higher is also the incident flux. This can explain the correlation between these parameters. Additionally a lower height of the primary X-ray source above the event horizon causes a significantly higher amount of gravitational redshift which also can cause correlation between these parameters. It is also visible that the second solution for very low lamppost heights does not influence the overall probability distribution in this two dimensional parameter space.
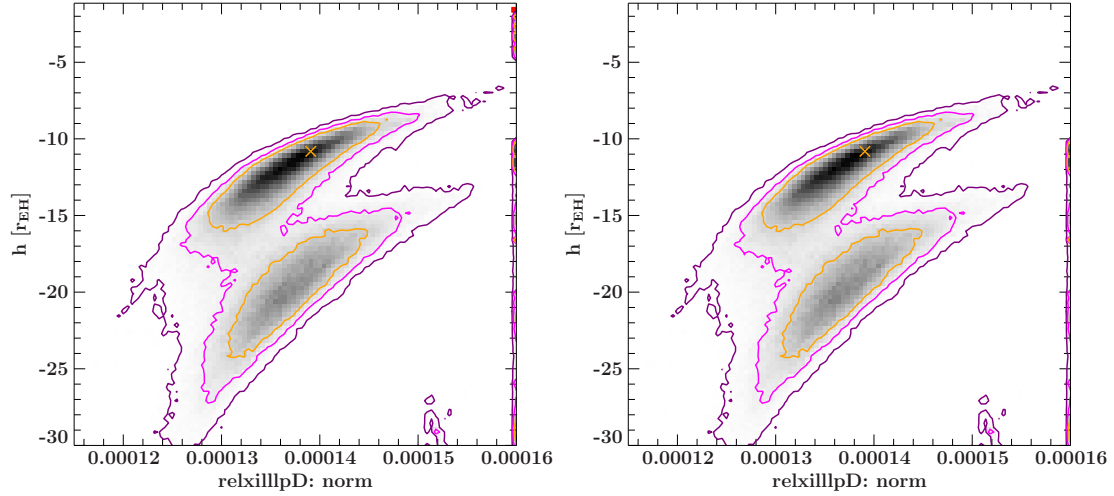
Figure 7.13: Error contours for the lamppost height h versus the normalization of the relxill model
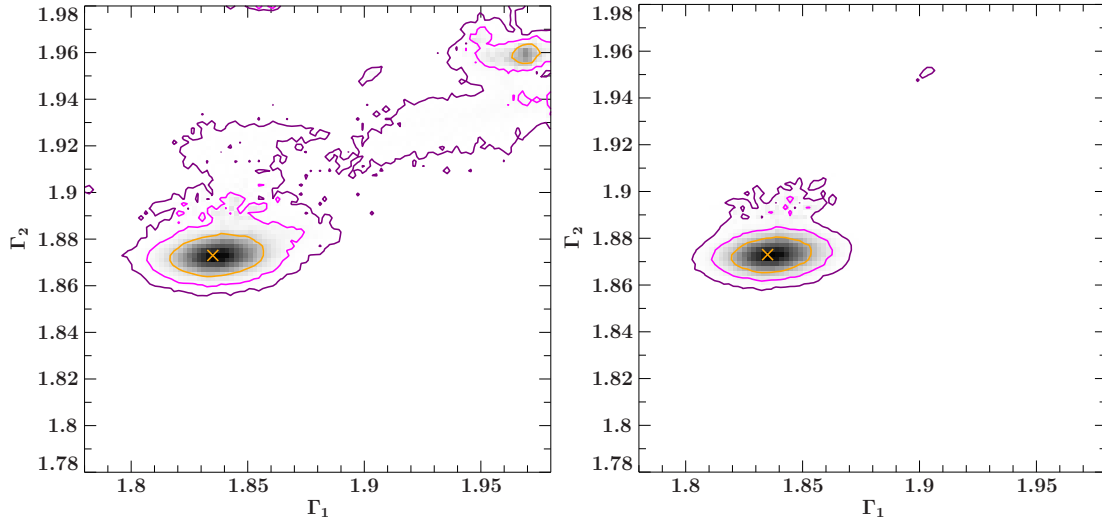
Figure 7.14: Error contours for the two photon indices Γ_1 and Γ_2

Photon indices

The two separate photon indices for *XMM-Newton* and *NuSTAR* are not correlated but there is a difference noticeable between the two possible solutions for different lamppost heights. The contour including all walkers shows another island of more than 99% confidence in the upper right corner, representing higher values for both photon indices. This island is not present for the separate solution for higher lamppost heights shown in the right panel. Also the region connecting the confidence interval including the highest confidence value with this separate island has some patches with more than 68% confidence. The cross calibration issue for the continuum emission as explained in section 5.3 is a possible explanation for these additional features.
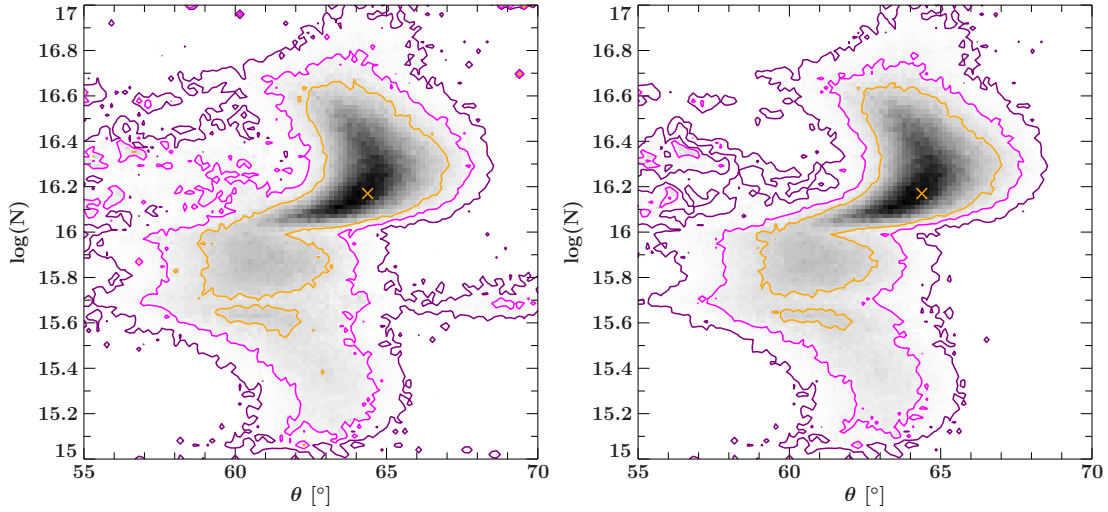
Figure 7.15: Error contours for the inclination i versus the density parameter $\log(N)$

Inclination and density parameter

Fig. 7.15 shows that there is a correlation present between the inclination i towards the accretion disk and the density parameter $\log(N)$ of the accretion disk.The region of confidence higher than $99\,\%$ covers a large interval of the density parameter with $15.6 \leq \log(N) \leq 16.6$. For the inclination the range is $59° \leq i \leq 68°$. It is remarkable that the solution for lower lamppost heights has no visible effect on this error contour.

Black hole spin and photon indices

The spin parameter a of the black hole gives different islands of high confidence with respect to the two photon indices Γ_1 and Γ_2 which can be seen in the upper and lower panel of Fig. 7.16 respectively. For values of $\Gamma_1 \sim 1.84$ and $\Gamma_2 \sim 1.87$ the black hole spin converges towards its theoretical upper limit. The other island of high confidence for $\Gamma_1 \sim 1.97$ and $\Gamma_2 \sim 1.96$ shows the highest probability of a at ~ 0.995 whereas the region with confidence higher than $99\,\%$ extends from $a \sim 0.989$ to $a \sim 0.996$. By removing all walkers of the solution for the low lamppost height the islands of high confidence for the higher photon indices also vanish. This suggests that a combination of a very low lamppost height, higher photon indices and a black hole spinning close to its but significantly lower than its theoretical maximal spin can give a similar parameter set as the other, more probable solution.

Lamppost height and density parameter

In Fig. 7.17 the confidence map of the lamppost height h versus the density parameter $\log(N)$ is shown. This parameter space is fairly complicated with multiple local minima. It shows that it is fairly difficult to find the parameter set which describes a given dataset best. Also the region of confidence higher than $99\,\%$ a fairly large region with $15.6 \leq \log(N) \leq 16.6$ and $8 \leq h \leq 24$. In addition this confidence map shows a large amount of red pixel around the border which correspond to single spikes which are not considered
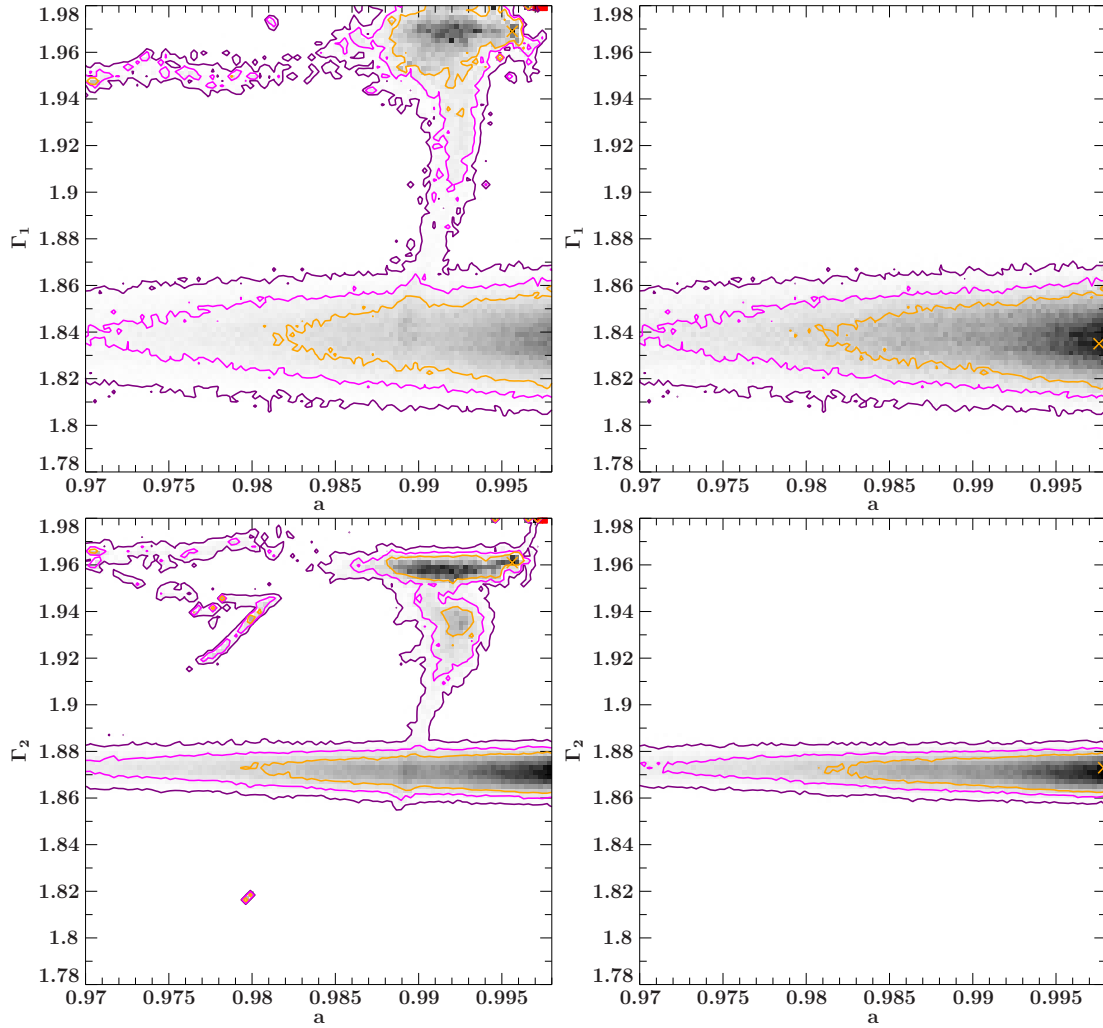
Figure 7.16: Error contours for the black hole spin a versus the two photon indices $\Gamma_{1/2}$

part of the actual confidence map but numerical instabilities of either the given model, the MCMC algorithm or the computing of the confidence map itself.

Density parameter and ionization state

The density of the accretion disk, represented by the density parameter $\log(N)$, and the ionization state of the material in the accretion disk, expressed in $\log(\xi)$, are expected to influence the spectrum generated by the relxill model in a similar way. This idea comes from the fact that lower ionization state but higher density can account for a similar amount of ionized atoms than a higher ionization state in the first place. So a correlation between these parameters is expected. In Fig. 7.18 the confidence map for both parameters is shown. It can be seen that there is some correlation present but the range of 99 % confidence for the ionization parameter is fairly narrow and also differs for the different solutions with different lamppost heights. In the right panel of Fig. 7.18 the solution for lower lamppost heights shows values of $2.74 \leq \log(\xi) \leq 2.88$ whereas for all
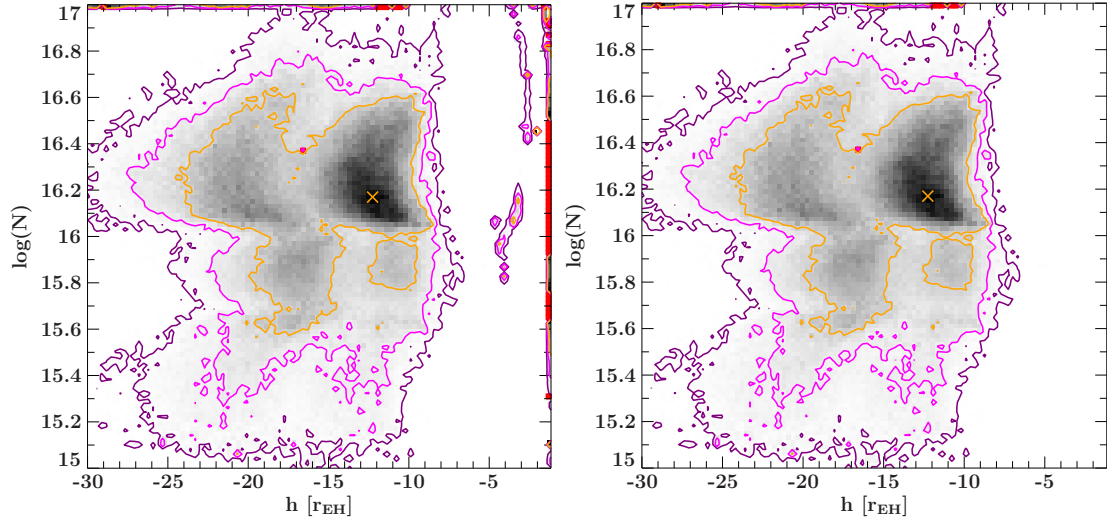
Figure 7.17: Error contours for the lamppost height h versus the density parameter $\log(N)$
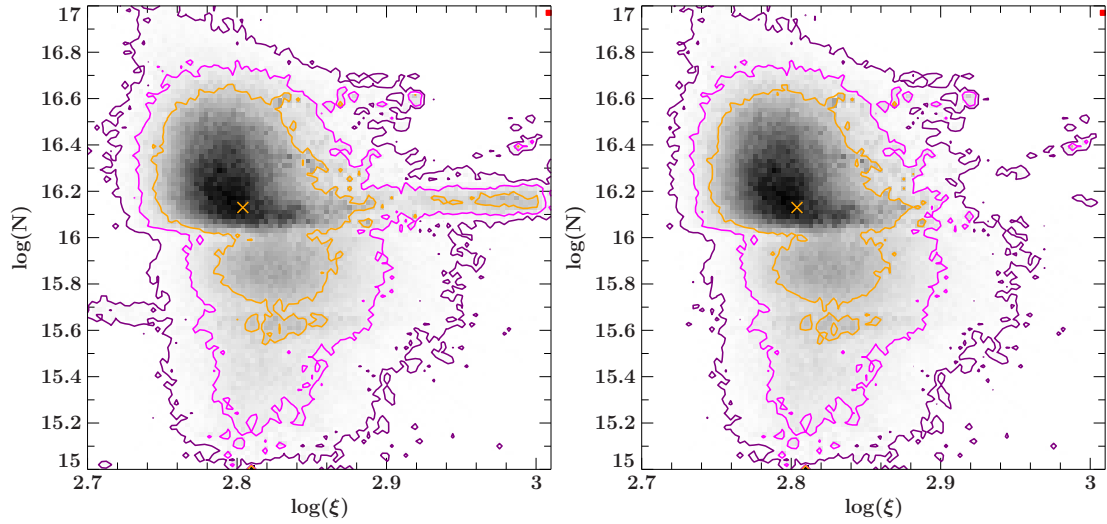
Figure 7.18: Error contours for the ionization state $\log(\xi)$ versus the density parameter $\log(N)$

walkers combined in the left panel there is a region present for $\log(N) \sim 16.15$ in which the high confidence interval reaches up to $\log(\xi) \sim 3.0$. Thus these values of high confidence correspond to the possible solution with a lower lamppost height h. In this map can also be seen that the parameter space is fairly complicated with multiple local minima and it is difficult to find the actual parameter combination which represents the data best.

8 Conclusions

8.1 Determination of the density parameter

The relxilllpD model is the first model with the ability to not only model common relativistic reflection features such as the black hole spin and the height of the primary X-ray source in the lamppost model but also the density of the accretion disk itself. Using the numerical method of Markov chain Monte Carlo we were able to map the probability distribution of the parameter space for the overall model and could determine the density of the accretion disk to be not $n = 10^{15}$ particles per cm^3 as assumed by older reflection models like xillver and the other relxill versions but rather higher, tending for this particular source of interest, Arakelian 120, to $n \sim 10^{16.12}$ particles per cm^3. However, the probability distribution function shows that there is no single best fit present for this parameter. In terms of parameter correlation the density of the accretion disk is only slightly correlated with the ionization state but there is correlation present between it and the inclination of the accretion disk towards the observer.

8.2 Numerical instabilities

Probability distributions for some parameters, for example the iron abundance A_{Fe} and the density parameter $\log(N)$, show a variety of sharp peaks. It is very unlikely that the probability indeed has very close local maxima at these points. The xillver model as described in García et al. (2013), and therefore also the relxill model as it is based on this, relies on grids of given densities and ionization states which are only calculated at certain points and then interpolated in order to cover the full parameter space. These support points in the grid can possibly cause the individual spikes seen in the probability distributions. However, it is also possible that the MCMC algorithm used to obtain the probability distributions in the first place is responsible for single peaks in these distributions.

8.3 Acceptance of the model

The acceptance fraction towards high number of iterations being ~ 0.029 in general is considered as the model not describing the data in a correct way. This suggests that the assumed lamppost structure might no represent what is observed. The application of relativistic reflection models like relxill is frequently discussed (see for example Porquet et al. (2017) for a very recent discussion about this source, or Matt et al. (2014) and Choudhury et al. (2017) for a comprehensive review of the particular model in use). Porquet et al. (2017) also suggest that another combination of processes being able to describe the observed spectrum in an acceptable manner is comptonization with two populations of seed photons with different temperatures. The first population might be located in the warm

and optically thick corona and the second one surrounding this and consisting of a hot and optically thin plasma.

Neither of both possibilities, relativistic reflection and additional comptonization, can be confirmed nor neglected. However the introduction of a model which can provide variation of the density parameter of the accretion disk is a big step towards a more accurate description of the processes in one of the most extreme environments in our universe.

References

Antonucci R., 1993, ARA&A31, 473

Bardeen J.M., 1970, Nature226, 64

Bevington P.R., Robinson D.K., 2003, Data reduction and error analysis for the physical sciences

Blandford R.D., Payne D.G., 1982, MNRAS199, 883

Blandford R.D., Znajek R.L., 1977, MNRAS179, 433

Bondi H., 1952, MNRAS112, 195

Burtscher L., Davies R.I., Graciá-Carpio J., et al., 2016, A&A586, A28

Choudhury K., Garcia J.A., Steiner J.F., Bambi C., 2017, ArXiv e-prints

Cowles M., Carlin B., 1996, Journal of the American Statistical Association 91, 883

Dauser T., 2010, Theoretical Modeling of Broad Emission Lines

Dauser T., 2014, Ph.D. thesis, FAU Erlangen Nuernberg

Dickey J.M., Lockman F.J., 1990, ARA&A28, 215

Einstein A., 1916, Annalen der Physik 354, 769

Fabian A.C., Ballantyne D.R., Merloni A., et al., 2002, MNRAS331, L35

Fabian A.C., Miniutti G., Gallo L., et al., 2004, MNRAS353, 1071

Fink M., 2016, *Master's thesis*, FAU Erlangen Nuernberg

Foreman-Mackey D., Hogg D.W., Lang D., Goodman J., 2013, PASP125, 306

Frank J., King A., Raine D.J., 2002, Accretion Power in Astrophysics: Third Edition

García J., Dauser T., Reynolds C.S., et al., 2013, ApJ768, 146

Gelman A., Roberts G.O., Gilks W.R., 1996, Bayesian Statistics 5, 599

Ghisellini G., Haardt F., Matt G., 2004, A&A413, 535

Gokus A., 2017, *Master's thesis*, FAU Erlangen Nuernberg

Goodman J., Weare J., 2010, Communications in Applied Mathematics and Computational Science, Vol. 5, No. 1, p. 65-80, 2010 5, 65

Gorenstein P., 2012, Optical Engineering

Harrison F.A., Craig W.W., Christensen F.E., et al., 2013, ApJ770, 103

Hastings W.., 1970, biometrika 57, 97

Ho L.C., 2002, ApJ564, 120

Houck J.C., Denicola L.A., 2000, In: Manset N., Veillet C., Crabtree D. (eds.) Astronomical Data Analysis Software and Systems IX, Vol. 216. Astronomical Society of the Pacific Conference Series, p. 591

Jansen F., Lumb D., Altieri B., et al., 2001, A&A365, L1

Kalberla P.M.W., Burton W.B., Hartmann D., et al., 2005, A&A440, 775

Kaviraj S., Laigle C., Kimm T., et al., 2017, MNRAS467, 4739

Kerr R.P., 1963, Phys. Rev. Lett. 11, 237

Krauss F., 2016, Ph.D. thesis, FAU Erlangen Nuernberg

Lightman A.P., 1974a, ApJ194, 429

Lightman A.P., 1974b, Ph.D. thesis, California Institute of Technology, Pasadena.

Matt G., Fabian A.C., Ross R.R., 1993, MNRAS264, 839

Matt G., Marinucci A., Guainazzi M., et al., 2014, MNRAS439, 3016

Metropolis N., Rosenbluth A.W., Rosenbluth M.N., et al., 1953, J. Chem. Phys.21, 1087

Miller J.M., Ballantyne D.R., Fabian A.C., Lewin W.H.G., 2002, MNRAS335, 865

Miller J.M., Tomsick J.A., Bachetti M., et al., 2015, ApJ799, L6

Miniutti G., Fabian A.C., Anabuki N., et al., 2007, PASJ59, 315

Mushotzky R.F., Done C., Pounds K.A., 1993, ARA&A31, 717

Netzer H., 2015, ARA&A53, 365

Nordgren T.E., Helou G., Chengalur J.N., et al., 1995, ApJS99, 461

Osterbrock D.E., Pogge R.W., 1985, ApJ297, 166

Pinto C., 2013, Ph.D. thesis, Radboud Universiteit Nijmegen

Piran T., 1978, ApJ221, 652

Porquet D., Reeves J.N., Matt G., et al., 2017, ArXiv e-prints

Pringle J.E., Rees M.J., Pacholczyk A.G., 1973, A&A29, 179

Reynolds C.S., Nowak M.A., 2003, Phys. Rep.377, 389

Rybicki G.B., Lightman A.P., 1986, Radiative Processes in Astrophysics

Schwarzschild K., 1916, Sitzungsberichte der Königlich-Preussischen Akademie der Wissenschaften, Sitzung vom 3. Februar 1916 186–196

Shakura N.I., 1973, Soviet Ast.16, 756

Sharma S., 2017, ARA&A55, 213

Sunyaev R.A., Truemper J., 1979, Nature279, 506

Tanaka Y., Nandra K., Fabian A.C., et al., 1995, Nature375, 659

Thorne K.S., 1974, ApJ191, 507

Urry C.M., Padovani P., 1995, PASP107, 803

Vaughan S., Fabian A.C., Ballantyne D.R., et al., 2004, MNRAS351, 193

Verner D.A., Ferland G.J., Korista K.T., Yakovlev D.G., 1996, ApJ465, 487

Wandel A., Peterson B.M., Malkan M.A., 1999, ApJ526, 579

Ward M., Elvis M., Fabbiano G., et al., 1987, ApJ315, 74

Wilms J., Allen A., McCray R., 2000, ApJ542, 914

Wilson A.S., Colbert E.J.M., 1995, ApJ438, 62

Wolter H., 1952, Annalen der Physik 445, 94

Acknownledgements

First of all I would like to thank my family for all the support. Without you I could not be where I am today. Next of course I would like to thank my advisor Jörn Wilms to let me the freedom of deciding how to address the topic presented in this work and for being a supportful person with high amount of patience in general. The same is true for Thomas Dauser who guided me not only into this topic but into the overall working procedure and who always has an open ear to spontaneous questions. Bastian Falkner offered a lot of advise regarding the MCMC algorithm, its implementation and ISIS in general, I am very thankful for that. I would like to thank Marco Fink for endless conversations not only about the work presented in this thesis and very specific questions about the source and the models but also about programming philosophies in general. Tobias Beuchert and myself often had very inspiring conversations about X-ray astronomy during our car rides back from Bamberg to Erlangen in the night, thank you for the nice time. I would like to say thank you to the whole admin team of the Remeis observatory, especially Ingo Kreykenbohm who is willing to share an office with myself and from whom I learnt a lot about how to deal with computers and networks in an effective and productive way. I also thank Simon Kreuzer, who is also part of the admin team, for the incredible amount of help to get used the job management system slurm without which I would not have been able to compute the results presented in this work. All of the admins offered me a high amount of trust by letting me change sensitive parts of the computer system, software and network configurations which was necessary to get the MPI implementation of MCMC working. I would like to say a very special thank you to Melanie Lang and Alexander Reichel. I have a really great time of studying physics with you and I am sure without you it would be hard for me to survive the time in the lecture halls. My good friend Gregor Lettowsky was the first person to show me how to deal with the GNU/Linux operating system. From this moment on I learnt a majority of my knowledge about this amazing system from you. Without your help I surely would not have been able to solve the very different kinds of problems appearing during my work, thank you a lot for all of this.

Letztendlich möchte ich mich bei Hans-Werner Neumann bedanken, meinem ehemaligen Physik Lehrer aus meiner Zeit am Gymnasium. Er hat als Erster mein Interesse an der Astronomie geweckt und mich vor allem durch sein W-Seminar über Astronomie in der Oberstufe zu diesem Studium mit dieser Fachrichtung inspiriert. Ihm verdanke ich die bisher größte Entscheidung meines Lebens richtig getroffen zu haben.

Eigenständigkeitserklärung

Hiermit bestätige ich, dass ich diese Arbeit selbstständig und nur unter Verwendung der angegebenen Hilfsmittel angefertigt habe.

_____

(Ort, Datum)

_____

Philipp Weber